



HAL
open science

Dynamic failure precursors in soft matter

Stefano Aime

► **To cite this version:**

Stefano Aime. Dynamic failure precursors in soft matter. Mechanics of materials [physics.class-ph]. Université Montpellier, 2017. English. NNT : 2017MONT011 . tel-01801958v2

HAL Id: tel-01801958

<https://theses.hal.science/tel-01801958v2>

Submitted on 14 Sep 2018

HAL is a multi-disciplinary open access archive for the deposit and dissemination of scientific research documents, whether they are published or not. The documents may come from teaching and research institutions in France or abroad, or from public or private research centers.

L'archive ouverte pluridisciplinaire **HAL**, est destinée au dépôt et à la diffusion de documents scientifiques de niveau recherche, publiés ou non, émanant des établissements d'enseignement et de recherche français ou étrangers, des laboratoires publics ou privés.



THÈSE

Pour obtenir le grade de
Docteur

Délivré par l'Université de Montpellier

Préparée au sein de l'école doctorale Information structure systèmes
Et de l'unité de recherche Laboratoire Charles Coulomb

Spécialité : **Physique**

Présentée par **Stefano AIME**

Dynamic failure precursors in soft matter

Soutenue le 14/09/2017 devant le jury composé de

M. Luca Cipelletti	Professeur, Université de Montpellier	Directeur de thèse
Mme Sylvie Cohen-Addad	Professeur, Université Pierre et Marie Curie	Président du jury
Mme Emanuela Del Gado	Professeur, Georgetown University	Rapporteuse
M. Thibaut Divoux	Chargé de recherche, CNRS	Examineur
Mme Laurence Ramos	Directrice de Recherche, CNRS	Co-directrice de thèse
M. Dimitris Vlassopoulos	Professeur, IESL-FORTH	Rapporteur



A Silvia e Giovanni

Contents

Ouverture	1
1 Motivation and State of Art	3
1.1 Objectives, originality and novelty	3
1.2 Historical excursus	11
1.3 State of the art	15
1.4 Outline of the thesis	46
2 Experimental Methods	49
2.1 Light Scattering	49
2.2 Rheology	59
I Light scattering under shear	69
3 A stress controlled shear cell for small-angle light scattering and microscopy	71
I Introduction	
II Setup	
III Setup characterization	
IV Tests with model samples	
V Dynamic light scattering under shear	
VI Conclusion	
4 Scattering signal from shear-induced nonaffine deformations	85
1 Introduction	
2 Materials and methods	
3 DLS for a sheared sample	
4 Conclusions	
II Colloidal gels	99
5 Structure, dynamics and viscoelastic properties	101
5.1 Introduction	101
5.2 Theoretical background	104
5.3 Material and methods	106
5.4 Results	108
5.5 Discussion	115

6	Microscopic dynamics and failure precursors of a gel under mechanical load	119
7	Irreversible dynamics under large amplitude oscillatory shear	127
7.1	Yielding transition in large amplitude oscillatory shear	127
7.2	Delayed yielding in LAOStress	133
7.3	Structural evolution under an oscillatory stress	135
7.4	Correlation echoes track plasticity across cycles	137
7.5	Discussion	141
III	Colloidal glasses	143
8	Dense microgel suspension: dynamics under shear	145
8.1	Introduction	145
8.2	Sample preparation	146
8.3	Structure and dynamics at rest	148
8.4	Rheology	151
8.5	Reversible and irreversible nonaffine dynamics	152
8.6	Conclusion	159
	General Conclusions and Perspectives	161
A	An efficient scheme for sampling fast dynamics at a low average data acquisition rate	173
1	Introduction	
2	Acquisition time scheme	
3	Materials and methods	
4	Results and discussion	
5	Conclusions	
B	A model for failure in thermoplastic elastomers based on Eyring kinetics and network connectivity	181
I	Introduction	
II	Materials and methods	
III	Experimental observations	
IV	Kinetic model	
V	Simulations	
VI	Conclusion	
	Bibliography	197

Ouverture

Most children learn early that things break, whether it is a stick excessively bent or a favorite toy dropped from sufficient height. Such events teach us that we have to protect our belongings from mechanical overload if we want to keep them safe. Nevertheless, it is with our greatest disappointment that from time to time we realize that our efforts were not enough: posters pinned to the wall fall down unexpectedly days after we accurately fixed them, and the cable of our laptop charger gets damaged after being bent several times. Yet, the poster appeared to be well fixed before, and the cable could safely withstand a few bending cycles without apparent damage.

Failure is the term conventionally used to indicate that something does not work anymore as it is supposed to do. Many little annoying examples demonstrate that failure is very often undesired, uncontrolled and unpredicted. This is all the more true for large scale catastrophic events, like the collapse of bridges or dams, but also geological events like snow avalanches, landslides or earthquakes. When such events happen, all of a sudden, the question that emerges is: *Why?* Which means: *For what reason?* but also: *Why then, not earlier nor later?* As a matter of fact, both questions are unanswered, and still challenge the mind of many scientists with widely different backgrounds, from geology and engineering to physics, chemistry and biology. Surprisingly, or maybe unsurprisingly, it turns out that what is so common in our daily experience is based on profound science that is not yet fully understood.

The complexity of failure mainly lies in its multiscale nature: a massive snow avalanche always arises from tiny cracks between snowflakes, and its origin cannot be fully understood without tracing back to them. Furthermore, accessing these microscopic events from which failure originates holds the promise of providing a means of predicting the collapse before its occurrence, which in most cases appears far too difficult, if not impossible, only looking at macroscopic observables. Any measurable feature anticipating failure, which is thus exploitable for its prediction, is called a precursor. Failure precursors do exist (for instance, animals behave differently before an earthquake, which indicates that they can feel it approaching), but detecting them and recognizing them in their role of precursors is extremely challenging, which explains the scarcity of successful works in this field so far. In fact, if it is now recognized that purely macroscopic approaches are doomed to fail, combining macroscopic and microscopic investigation is still far from trivial, for several reasons that will be discussed in chapter 1.

In this work we present one of the first successful attempts to measure microscopic failure precursors in model soft solids. Here, microscopic plasticity under shear is observed using a novel setup, presented in part I, coupling a custom-made stress controlled shear cell to small angle static and dynamic light scattering. The main results come from the study of a colloidal gel, and will be discussed in part II, whereas in part III the generality of those results is examined by comparing them with a colloidal glass.

Motivation and State of Art

Contents

1.1	Objectives, originality and novelty	3
1.1.1	Material failure in our everyday life	3
1.1.2	Failure in soft materials	5
1.1.3	Key questions	6
1.1.4	Challenges	9
1.2	Historical excursus	11
1.3	State of the art	15
1.3.1	Steady-rate experiments	15
1.3.2	Creep experiments	20
1.3.3	Dynamic fatigue test	32
1.3.4	Conclusion	45
1.4	Outline of the thesis	46

1.1 Objectives, originality and novelty

1.1.1 Material failure in our everyday life

Material failure is ubiquitous on length scales ranging from a few nanometers, as in fracture of atomic or molecular systems [Weibull 1939, Célerié 2003] up to geological scales, as in earthquakes [Myers 2001, Ben-Zion 2008]. While some attempts have been made to harness failure, e.g. in order to produce new materials with a well controlled patterning [Nam 2012], material failure remains in general an unwanted, uncontrolled and unpredictable process. Indeed, a better control of the conditions under which material failure may or may not occur and the detection of any precursors that may point to incipient failure are the Holy Grail in many disciplines, from material science [Amon 2013, Guarino 2002, Pradhan 2005, Vinogradov 2012, Koivisto 2016] and biology [Bell 1978, Erdmann 2004, Buehler 2009, Gobeaux 2010] to engineering [Bazant 1991] and geology [Jones 1979, Sommerfeld 1982, Swanson 1983, Sommerfeld 1983, Voight 1988,

McGuire 2005, Wu 2006, Ancey 2007, Duputel 2009, Van Herwijnen 2011a, Van Herwijnen 2011b, Kato 2012, Johnson 2013, Bouchon 2013, Kromer 2015, Agioutantis 2016]

Failure may occur almost instantaneously, as a consequence of an impulsive load [Field 2004]: in this case the main interest typically consists in evaluating the damage as a function of impact speed and energy [Richardson 1996, Camacho 1996, Ball 1999]. Often, however, it manifests itself in more elusive ways, as in the sudden, catastrophic breakage of a material submitted to a constant or cyclic load, where failure may be preceded by a long induction time with little if any precursor signs of weakening [Basquin 1910, Andrade 1910]. In the latter case, sometimes referred to as dynamic fatigue failure [Kahn 2004], one has the possibility to monitor the stroboscopic evolution of micro to mesoscopic damage developing before macroscopic failure [Ewart 1986, Patra 2016], whereas such a detection is much more delicate in the former case.

Delayed failure under a constant load has been reported in a wide spectrum of phenomena, from large scale systems such as earthquakes [Lockner 2002, Ōnaka 2013], rock sliding [Kromer 2015], snow avalanches, [Reiweger 2010] and structural materials [Bazant 1991, Maekawa 2016] to small scale ones such as biological materials [Bell 1978, Erdmann 2004, Gobeaux 2010] relevant to bioengineering [Anwar 2009]. Other examples include crystalline [Poirier 1985] solids like metals [Troiano 1959, Nakasato 1980, Golub 2003], ice [Ashby 1985, Sinha 1988] or colloidal polycrystals [Bauer 2006], as well as composite materials such as wood [Guarino 2002], paper [Koivisto 2016] or synthetic fibers [Nechad 2005b], and amorphous systems [Preston 1942, Gurney 1947, Aoki 1980], including viscoelastic soft materials [Gopalakrishnan 2007, Gibaud 2010, Divoux 2011, Siebenbürger 2012, Grenard 2014, Sentjabrskaja 2015], such as adhesives [Sancaktar 1985] and network-forming materials [Bonn 1998, Poon 1999, Skrzyszewska 2010, Sprakel 2011, Leocmach 2014].

The widespread occurrence of delayed failure represents a challenge for the durability of objects and structures, a well known problem in civil engineering [Bazant 1991]. In order to design durable applications, structural parameters have to be optimized, which requires control of the material lifetime under realistic conditions. Conversely, knowledge about the stress required to trigger failure and flow is relevant in other applications, from industrial processing to oil extraction and transportation, where engineers face the well known problem of pipe clogging [Zuriguel 2015, Van de Laar 2016, Koivisto 2016]. Thanks to the power of modern simulation schemes, nowadays such knowledge can often be considered satisfactory for applications, but it remains essentially empirical and system-specific: much still has to be done in order to achieve a unitary description of those phenomena.

At the same time, diagnosis of mechanical faults on existing structures is required in order to assure proper maintenance [Collacott 1977]. This is extremely important not only in civil engineering, where the catastrophic collapse of bridges, dams or buildings still represents a relevant origin of casualties, but also in the transportation industry, as in railway maintenance or in aircraft industry, where maintenance is delicate and expensive. As an example, more than 60% of the total ownership costs for US aviation

are represented by aircraft maintenance, due to inefficient Condition Based Maintenance (CBM) system [Bell 2008].

On a still larger scale, the detection of precursors of catastrophic events such as earthquakes, rockslides, landslides, snow avalanches or volcano eruptions is certainly of paramount importance for many self-evident social, economical and environmental reasons. It has been argued [Sommerfeld 1982, Voight 1988, Bouchon 2013, Kromer 2015] that this prediction might be achieved, and indeed in 1975 the Chinese Seismological Bureau successfully predicted a magnitude 7.3 earthquake [Jones 1979]. However, despite the optimistic wave generated by such successful prediction, to the best of our knowledge this remains the only documented example, although *a posteriori* analyses could in some cases identify detectable precursors [McGuire 2005, Duputel 2009, Van Herwijnen 2011b, Kato 2012].

1.1.2 Failure in soft materials

Because of the outstanding relevance for many applications and its interest from a fundamental point of view, material failure represents a very active field of research, which has the interesting feature of being multidisciplinary, arousing the curiosity of researchers with widely different backgrounds.

In particular, material failure is relevant to soft matter physics, where the typical energy scale governing interactions between particles is of the order of thermal energy: for this reason, soft materials are generally characterized by large mechanical susceptibilities, and they respond to small or moderate stresses with large deformations, often displaying yielding and failure under a suitable range of applied stresses. Typical examples include emulsions [Liu 1996, Mason 1996], foams [Kabla 2007, Cohen-Addad 2013, Dallet 2014], polymer gels [Bonn 1998, Baumberger 2006, Skrzyszewska 2010, Karobi 2016], and suspensions of colloidal particles, quenched out of equilibrium because of crowding [Siebenbürger 2012, Sentjabrskaja 2015] or of the presence of attractive interactions [Poon 1999, Gopalakrishnan 2007, Gibaud 2010, Sprakel 2011, Grenard 2014].

Because of its widespread occurrence, failure in soft materials has strong implications for many everyday life and industrially relevant problems, including the processing of food [Van Vliet 2013], such as gluten [Ng 2008], starch [Vliet 1995], dough [Moraireira 2011], gelatine [McEvoy 1985, Groot 1996], thickeners [Ma 1996, Jaishankar 2014], yogurt [Leocmach 2014], and cheese [Faber 2017b], or biomaterials, such as living cells [Desprat 2005, Kollmannsberger 2011], tissues [Bell 1978], biopolymer networks [Wagner 2006, Janmey 2007, Gobeaux 2010] or protein assemblies [Liu 2007, Lieleg 2010, Brenner 2013].

Soft materials are excellent systems to investigate material failure, because their characteristic time and length scales are more readily accessible to experiments as compared to those of atomic systems: this opens the way to a detailed structural and dynamical characterization both before and after failure occurs. Moreover, a large variety of soft sys-

tems with a wide spectrum of interactions and structural and dynamical characteristics are available, thus allowing one to pinpoint the key parameters controlling the observed phenomena, possibly unveiling general behaviors. For these reasons, the emerging analogies between soft and hard materials [Schmoller 2013, Keshavarz 2017] make soft materials an ideal benchmark to investigate how a mechanical stress impacts condensed matter. Finally, the increasing relevance of soft materials in everyday life, as well as in industrial processes like for example in food industry [Stokes 2012, Spagnolie 2015, Faber 2017a] further alimnts the interest in a deeper understanding of their behavior under stress.

1.1.3 Key questions

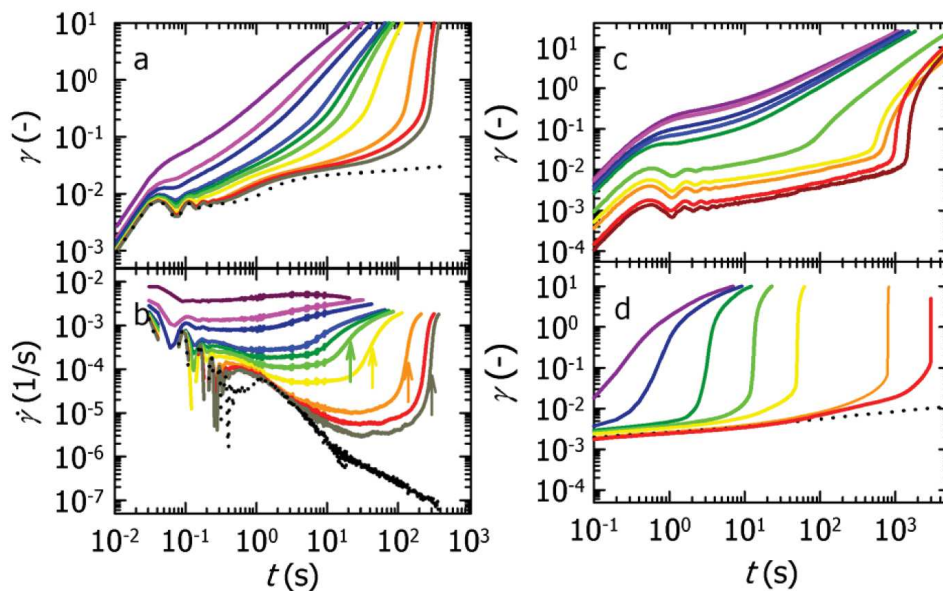


Figure 1.1: (a) Creep response of 8 wt% carbon black gel under a constant stress σ decreasing from left to right and (b) corresponding shear rate $\dot{\gamma}$. (c) Creep curves for a weak depletion gel of polystyrene particles and (d) for thermoreversible stearylated silica gels. Extracted from [Sprakel 2011].

Figure 1.1 illustrates an example of the delayed failure events that we address in this work. The sample is submitted to a constant mechanical shear stress that is applied at time $t = 0$, and it undergoes a very fast, solid-like deformation, followed by a so-called creep regime where the shear strain γ grows sublinearly, either logarithmically or as a power-law of time [Cottrell 1952]. Remarkably, this regime may last even hours, depending on the applied stress, until it is suddenly interrupted by a sharp increase in γ signaling material failure and the onset of flow.

The effects of failure are obvious at the macroscopic scale, and yet the dynamics that lead to such failure are governed entirely by the material's behavior at the smallest scales. Thus, to better understand the observed delayed onset of flow, we start investigating the

microscopic processes governing creep. Interestingly, although the ultimate fate of the material (formation of shear bands, ductile vs fragile fracture, permanent vs reversible damage) may differ according to the system, the macroscopic behavior before failure is quite general, as one can see by comparing the three samples investigated in Fig. 1.1.

Power-law creep is widespread in both crystalline and amorphous materials, however in the former case it is well understood and attributed to defect motion [Andrade 1910, Cottrell 1952, Poirier 1985, Miguel 2002], whereas in the latter case its microscopic origin remains controversial. Indeed it has been attributed in turn to the accumulation of irreversible, plastic rearrangements [Nechad 2005b, Caton 2008, Coussot 2006, Siebenbürger 2012, Sentjabrskaja 2015, Karobi 2016], to linear viscoelastic relaxation processes [Balland 2006, Gobeaux 2010, Leocmach 2014], or to a combination of both [Jagla 2011, Kun 2003], with different authors holding contrasting views on similar systems [Jagla 2011, Nechad 2005b].

For this reason, the first question that we want to answer with our work is the following: **What is the nature of the microscopic dynamics during the creep regime?**

More precisely, we want to understand if the power-law creep of amorphous systems is governed by the same irreversible microscopic processes evoked for crystalline solids, or if for those viscoelastic materials other deformation mechanisms are allowed, not necessarily implying structural damage, as it has been suggested for widely different systems, from biomaterials such as cells [Fabry 2001, Djordjevic 2003, Desprat 2005, Balland 2006, Kollmannsberger 2011, Hecht 2015], tissues [Kohandel 2005, Davis 2006, Freed 2006, Sinkus 2007, Klatt 2007, Shen 2013, Bentil 2014], or biopolymer networks [Amblard 1996, Gobeaux 2010, Patricio 2015] and pastes [Józwiak 2015], to food materials [Ma 1996, Zhou 1998, Goh 2003, Subramanian 2006, Caggioni 2007, Ng 2008, Korus 2009, Moreira 2011, Ronda 2013, Xu 2013, Jaishankar 2014, Leocmach 2014, Faber 2017a, Faber 2017b], colloidal gels [Grenard 2014] and polymer gels [Hung 2015, Lidon 2017], melts [Plazek 1960, Cherièrè 1997, Friedrich 1999, Hernández-Jiménez 2002, Metzler 2003], elastomers [Curro 1983] and composites [Metzler 1995].

Crucially, a detailed understanding of the creep regime holds the promise of unveiling the origin of the sudden failure of the material, potentially revealing any precursor signs of failure, which are difficult to detect by monitoring macroscopic quantities, such as the deformation rate [Koivisto 2016]. For this reason, the second question that we plan to answer with our work is the following: **How does the microscopic dynamics change as failure is approached? Could such evolution provide a means to detect an incipient failure?**

In order to properly address these questions, a different experimental protocol, represented in Fig. 1.2, can also be usefully employed, where yielding is not observed under constant stress, but under an oscillating stress (or strain, as in Fig. 1.2) with increasing amplitude. In such experiments, one typically observes a first linear regime, in the limit of small deformations, where the stress grows linearly with strain amplitude and the so-called viscoelastic moduli are independent of deformation. In this regime, linear rheology teaches us about the mechanical properties of the *unperturbed* sample, which in the case

of Fig. 1.2 is predominantly solid. However, when the sample is driven far enough from equilibrium (beyond γ_c in Fig. 1.2) it develops an amplitude-dependent response, with a growing loss modulus, which indicates that additional, nonlinear dissipative processes are triggered by the imposed deformation. Such processes become increasingly relevant at still higher amplitudes, and concomitantly the elastic modulus decreases, up to a point where the two moduli cross each other, so that in the large amplitude limit (beyond γ_f in Fig. 1.2) the mechanical response will be dominated by the loss modulus, showing that the initially solid-like material was fluidized by the applied deformation. Interestingly, this transition can be grasped as well by the stress vs. strain curve, which displays a clear crossover (around γ_y in Fig. 1.2) between the initial linear regime and the shear-thinning regime observed at larger amplitudes.

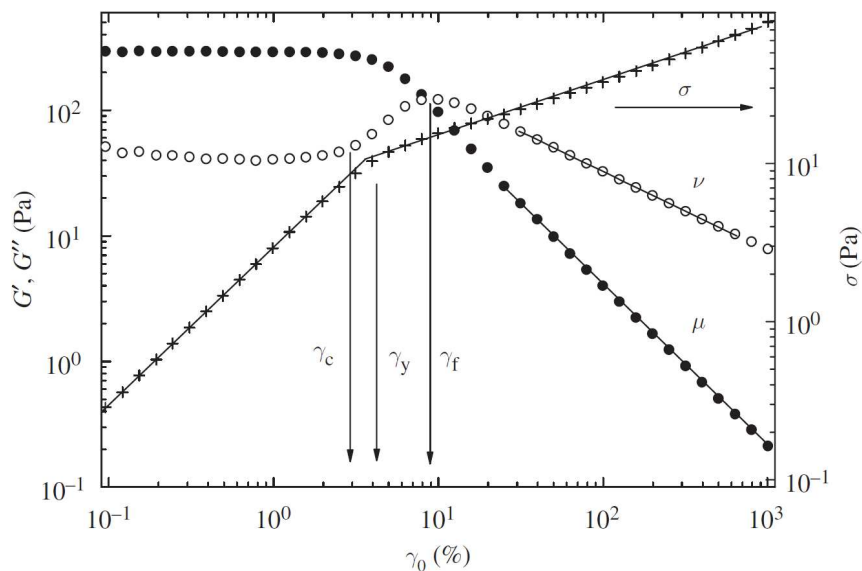


Figure 1.2: Circles, left axis: viscoelastic moduli G' (filled) and G'' (empty) for different values of the imposed strain amplitude γ_0 . Crosses, right axis: amplitude of the stress response as a function of strain. The vertical arrows indicate the end of the linear regime (strain γ_c), the onset of (viscoplastic) yielding (strain γ_y) and complete fluidization, that is, liquid-like response (strain γ_f). The sample is a star polymer solution. Extracted from [Christopoulou 2009].

The qualitative features observed in Fig. 1.2 seem to be quite general, being observed in a variety of soft systems like polymer solutions [Tirtaatmadja 1997], composites [Payne 1963], emulsions [Mason 1996, Bower 1999, Knowlton 2014], as well as colloidal gels [Raghavan 1995, Raghavan 1997, Yziquel 1999, Christopoulou 2009, Gibaud 2010, Kim 2014, Perge 2014, Moghimi 2017], glasses [Derec 2003, Petekidis 2003, Craciun 2003, Pham Trong 2008, Carrier 2009, Rogers 2011, Koumakis 2013, Hima Nagananasa 2014] and polycrystals [Louhichi 2015], whereas some other systems show a characteristic two-step yielding process, with a peculiar intermediate regime between

the onset of the nonlinear regime and the complete fluidization [Altmann 2004, Helgeson 2007, Pham Trong 2008, Koumakis 2011, Laurati 2014, Agrawal 2015, Brunel 2016].

Oscillatory yielding of soft solids has been rationalized by various models [Sollich 1998, Derec 2003, Miyazaki 2006, Carrier 2009, Radhakrishnan 2016], based on the idea that sample relaxation dynamics are essentially unperturbed by small amplitude shear, whereas the appearance of stress-induced plastic rearrangements determines the onset of the nonlinear regime at amplitudes beyond a given threshold. However, such threshold appears to be difficult to define unambiguously [Bonn 2017], as one can appreciate from the difference between γ_c , γ_y and γ_f in Fig. 1.2. In the attempt to investigate more deeply the nature of such yielding transition, recent experiments have addressed the microscopic reversibility of the imposed deformation, by detecting the onset of irreversible particle displacements either with direct imaging techniques [Pouliquen 2003, Marty 2005, Slotterback 2012, Keim 2014, Knowlton 2014, Hima Nagamanasa 2014], with scattering techniques, [Petekidis 2002a, Gibaud 2010, Amon 2013, Rogers 2014, Laurati 2014, Leheny 2015, Agrawal 2015], or in computer simulations [Regev 2015, Kawasaki 2015, Priezjev 2016, Priezjev 2017]. A transition from reversible to irreversible dynamics is indeed retrieved, although at a more detailed analysis the results appear rather controversial, and no consensus is found about the nature of this crossover, which has been described either as a smooth change [Keim 2013], a sharp crossover [Knowlton 2014, Kawasaki 2015] or a continuous nonequilibrium phase transition [Hima Nagamanasa 2014].

The possibility of bridging the gap between the (ir)reversible nature of microscopic dynamics and the macroscopic deformation makes oscillatory shear the ideal technique to precise and complete the first two questions. Therefore, in line with the recent work mentioned above, the third question that we plan to answer with our experiments is the following: **Which microscopic processes govern the reversible to irreversible transition observed upon yielding? How are they related to the change in rheological properties?**

1.1.4 Challenges

In order to address the above questions, several challenges have to be faced, essentially coming from the intrinsically multiscale nature of material failure [Ben-Zion 2008, Ritchie 2011], involving collective behaviors spanning characteristic energy, time and length scales from the constitutive elements to the system as a whole. Therefore, the essential challenge is to bridge over those scales. This is typically challenging in simulations, where computational performance sets severe limitations to the total number of unitary elements that can be simulated at once [Colombo 2014, Landrum 2016]. Incidentally, most numerical simulation schemes are currently implemented in a strain-controlled fashion, which is not adapted to capture the creep dynamics. In order to access realistic volumes, coarse grained models are available, like mesoscopic elastoplastic models

[Bocquet 2009, Martens 2011], the fuse model [De Arcangelis 1985, Sornette 1992], the fiber bundle model [Daniels 1945, Pradhan 2010] with its many modifications [Pradhan 2002, Pradhan 2003, Kun 2003, Kun 2008, Kovacs 2008, Baxevanis 2007, Jagla 2011], and finite element models [Fragiacomo 2004], even though most of them were developed to describe hard materials [Sornette 1992, Fragiaco 2004, Kun 2007] and do not contain thermal fluctuations, which might be relevant in softer materials like the ones we investigate. A different implementation of such elasto-plastic models is presented in appendix B as a way to describe thermoplastic elastomers [Aime 2017]. Another delicate point concerning coarse grained numerical simulations is that they rely on specific assumptions on the fundamental mechanisms governing the macroscopic deformation. As a consequence, even once the rheological behavior is correctly reproduced, the link between the information obtained at the mesoscopic scale and the physical mechanisms governing the real systems might not be straightforward. An example is again the debate on power-law creep, which is equally reproduced by numerical models built on fairly different assumptions [Pradhan 2002, Jagla 2011].

Bridging different length and timescales is also challenging for experiments, as it is well known by geologists struggling to predict earthquakes [McGuire 2005] and snow avalanches [Van Herwijnen 2011b], since the precursor of such macroscopic events is very likely to be represented by tiny, fast events occurring at the microscopic scale after a potentially long, unpredictable waiting time. In the present work we mainly address the above questions with experiments, by imposing a well-controlled load to the sample and by measuring simultaneously both its mechanical response and its microscopic dynamics. Such simultaneous measurements are quite rare [Chen 2010] and mostly restricted to rheo-microscopy (the coupling of a rheometer and a microscope) [Van der Linden 2003, Besseling 2009] or rheo-DWS (the coupling of a rheometer and a dynamic light scattering apparatus working in the multiple scattering regime) [Wagner 1998, Hébraud 1997]. Although both techniques represent an invaluable extension of standard rheology, they have different limitations that might make them unfit to our purposes. For example, real space measurements, like microscopy, suffer an intrinsic trade-off limiting the total volume that can be probed at a given rate and a given spatial resolution. On the other hand, diffusing wave spectroscopy (DWS) can effectively probe extremely small displacements (down to the nanometer scale) in macroscopic samples (several centimeters), but its main disadvantage is the lack of a direct connection between the observed signal and the nature of the probed displacements. To overcome these limitations, in our experiments we will mainly use time-resolved dynamic light scattering, a technique described in chapter 2, which will allow us to detect rearrangements involving motion on a very small scale - down to a fraction of μm -, while being able to probe a fairly large portion of the sample, up to some mm in (linear) size. On the other hand, investigating the microscopic dynamics of a sample under shear with dynamic light scattering is also challenging, since the physically interesting signal has to be decoupled from the trivial contribution coming from the so-called affine deformation of the sample. This requires a careful, nonstandard analysis of the light scattering signal (discussed in chapter 4), which proves in addition to

be very sensitive to the presence of eventual wall slip or shear banding, another positive side effect of dynamic light scattering.

A last nontrivial challenge is represented by imposing a well-controlled stress to the sample. From established works in literature (cf. e.g. Fig. 1.1) we know that delayed failure is highly stress dependent, so that we require that stress should be homogeneous in the sample. Among the deformation geometries commonly employed in mechanical testing, cone-plate rheology is the only one satisfying this requirement [Macosko 1994]. However, such a deformation geometry is particularly difficult to couple with light scattering, because of the optical quality of the conical surface. By contrast, rheo-optical setups are often based on plate-plate torsional rheometry, in which case the applied stress is far from being homogeneous. In order to meet both requirements of optical quality and stress uniformity we decided to work in a different shear geometry, with parallel sliding planes. To this aim, we realized a stress controlled shear cell, which will be described in chapter 3.

1.2 Historical excursus

"Dicebat Bernardus Carnotensis nos esse quasi nanos, gigantium humeris insidentes, ut possimus plura eis et remotiora videre, non utique proprii visus acumine, aut eminentia corporis, sed quia in altum subvenimur et extollimur magnitudine gigantea" (John of Salisbury, *Metalogicon*). The medieval image, reported by John of Salisbury, is particularly adapted to introduce a brief survey of the current knowledge around the topics that will be touched by this work. In English it would read: "Bernard of Chartres used to say that we [the Moderns] are like dwarves perched on the shoulders of giants [the Ancients], and thus we are able to see more and farther than the latter. And this is not at all because of the acuteness of our sight or the stature of our body, but because we are carried aloft and elevated by the magnitude of the giants" [Trojan 2004].

Although it is easy for us, modern scientists, to identify with this medieval image (Newton himself used it in a letter to Robert Hooke), we can linger on it, asking ourselves what exactly gives us our raised viewpoint. There is no doubt that the incredible amount of easily accessible information, which was unimaginable already 30 years ago, together with the improved data quality provided by modern scientific instruments and ever-increasing computational schemes and platforms, constitutes an absolutely favorable working condition for today's soft matter scientists. However, there is also another related aspect, which I would like to take as a starting point. To introduce it, another quotation will help, this time from C.S. Lewis, who writes that *"The universe rings true whenever you fairly test it"* [Lewis 1955]. This is specially true in science, being clear that to simply test is not enough: one has to do it fairly in order to obtain a true answer, and history has shown how long and curvy is the path through which we learn how to fairly test universe, and to ask relevant scientific questions in the proper way. If on the one hand this is necessarily the path of every young scientist wishing to become an adult scientist,

on the other hand this path is traced by the example of curious people that across the centuries have found out better ways to formulate scientific questions, and more proper ways to test them. The beginning of this work is dedicated to a short selection of those curious people, with particular focus on the research on material failure.

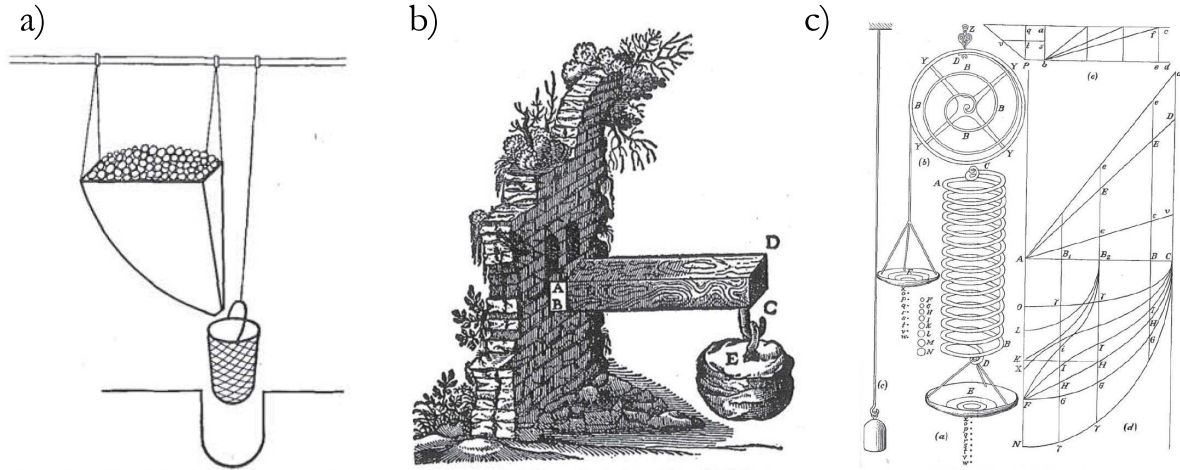


Figure 1.3: Schemes of the mechanical tests designed by (a) Leonardo da Vinci, (b) Galileo Galilei and (c) Robert Hooke. Extracted from [Timoshenko 1953].

Without any doubt, the dawn of this research dates back to ancient times: from the earliest times when people started to build, it was found necessary to have information regarding the strength of structural materials, so that rules for determining safe dimensions of building elements could be drawn up. Ancient civilizations as Egyptians, Greeks and Romans certainly had some empirical rules of this kind, since without them it would have been impossible to erect their great monuments, some of which still exist [Timoshenko 1953]. However, to the best of our knowledge, the first documented attempt to directly address the strength of structural materials with dedicated experiments is attributed to Leonardo da Vinci, in XV century [Parsons 1976]. In his note "Testing the Strength of Iron Wires of Various Lengths" he gives the sketch of the first tensile experiment of human history (Fig. 1.3a) and remarks: *"The object of this test is to find the load an iron wire can carry. Attach an iron wire [...] to something that will firmly support it, then attach a basket [...] to the wire and feed into the basket some fine sand through a small hole placed at the end of a hopper. A spring is fixed so that it will close the hole as soon as the wire breaks. [...] The weight of sand and the location of the fracture of the wire are to be recorded. The test is repeated several times to check the results. Then a wire of one-half the previous length is tested and the additional weight it carries is recorded; than a wire of one-fourth length is tested and so forth, noting each time the ultimate strength and the location of the fracture"* [Da Vinci 1972]. Besides the same idea of conceiving an *ad hoc* experiment to test the strength of a wire, independently from its application, which is certainly the most revolutionary aspect of Leonardo's approach, two interesting points have to be noted in his description of the experiments: first, one single

test is not enough, since its result has to be checked by several repetitions, suggesting that Leonardo had the intuition that statistics are particularly relevant for those phenomena. Five centuries afterwards, the work of Waloddi Weibull [Weibull 1939] will rationalize this concept in mathematical terms. Second, Leonardo understood that the length of the wire plays a role, longer wires carrying less load, which is indeed the starting point of Weibull model, namely that real wires are heterogeneous, so that longer wires are more likely to contain a critical defect [Lund 2001].

With a different accent, the question about the relationship between size and strength was also addressed by Galileo Galilei at the beginning of XVII century. In his book "Discorsi e dimostrazioni matematiche intorno a due nuove scienze", he investigates the strength of materials in simple tension, like in Leonardo's experiments, and he states that the strength of a bar is proportional to its cross-sectional area and independent of its length: this defines, for Galileo, the "absolute resistance to fracture". With respect to Leonardo's results, this remark suggests that Galileo worked with thicker and more homogeneous materials, whose strength did not display marked size dependence. Having the absolute resistance of a bar, Galileo then turns to a different experiment in which the resistance of the same bar is tested in bending geometry (Fig. 1.3b). By analyzing the deformation profile, he finds that geometrically similar bars are not equally strong, as the bending moment increases as the square of the length, whereas the resisting moment increases as the cube of the radius: thus, to keep the strength constant, the cross-sectional dimensions must be increased at a greater rate than the length. For this reason, he argues, *"you can plainly see the impossibility of increasing the size of structures to vast dimensions either in art or in nature; likewise the impossibility of building ships, palaces, or temples of enormous size [...]; nor can nature produce trees of extraordinary size because the branches would break down under their own weight. [...] Indeed, the smaller the body the greater its relative strength"* [Galilei 1638]. We see that the use of mathematics to rationalize his findings and the extrapolation, from the particular experiment, of a general result applicable to different systems characterizes Galileo's approach to material failure. For this reason, Galileo's work represents the beginning of the science of solid mechanics [Timoshenko 1953].

Later in XVII century, this new-born science evolved rapidly thanks to the contribution of Robert Hooke, who is rightfully considered the father of the theory of elastic bodies. In his manuscript "De potentia Restitutiva", Hooke explains the linear relationship between elastic force and spring deformation, which is also known as Hooke's law: *"Take a wire string [...] and fasten the upper part thereof to a nail, and to the other end fasten a scale to receive the weights: then with a pair of compasses take the distance of the bottom of the scale from the ground or floor underneath, and set down the said distance, then put in weights into the said scale and measure the several stretchings of the said string, and you will find that they will always bear the same proportions one to the other that the weights do that made them"*. By investigating other deformation geometries like torsion, bending and compression (Fig. 1.3c) he comes to the following general conclusion: *"It is very evident that the Rule or Law of Nature in every springing*

body is, that the force or power thereof to restore itself to its natural position is always proportionate to the distance or space it is removed therefrom" [Hooke 1678].

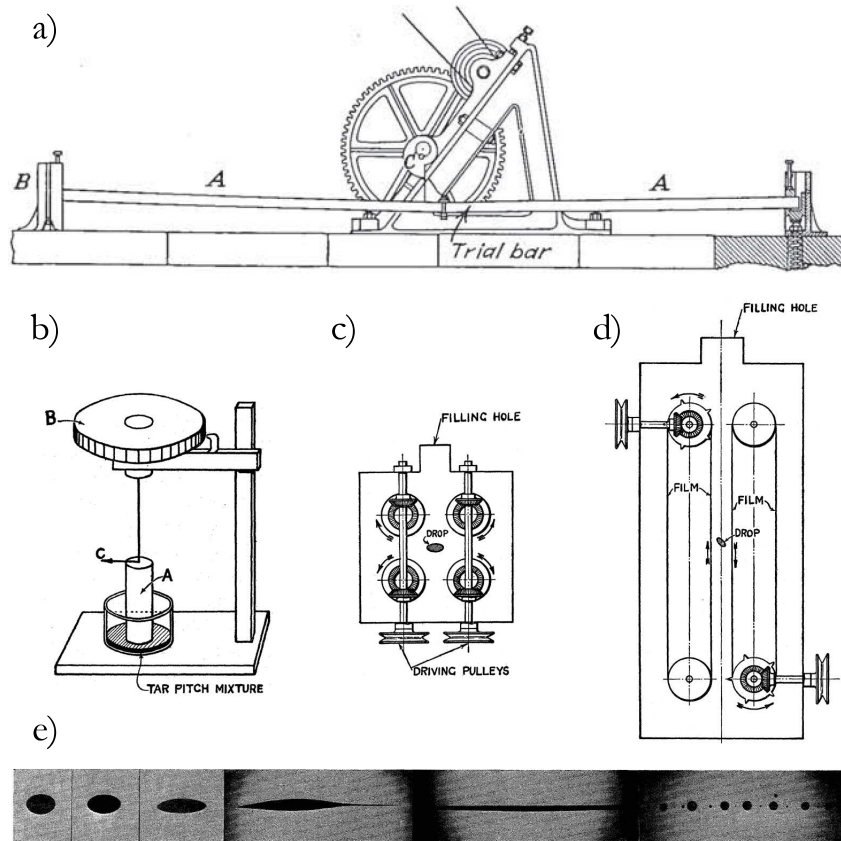


Figure 1.4: (a) James and Galton's fatigue-testing machine: a rotating eccentric is used to deflect and release the bar, with a frequency from 4 to 7 rpm [Timoshenko 1953]. (b) Torsional rheometer used by Taylor [Taylor 1934] to measure the viscosity of "highly viscous" (presumably viscoelastic) fluids. (c-d) Rheo-optical cells to visualize the deformation of a viscoelastic drop under biaxial deformation (c) and shear deformation (d). (e) Destabilization of a viscoelastic drop under biaxial deformation [Taylor 1934].

From seventeenth century to the modern era, contributions to this field, specially on the mathematical formulation of the theory of elasticity with the new instruments provided by infinitesimal calculus, are numerous. Mentioning most of them would largely go beyond the purpose of this section. However, it is fascinating to follow the close connection between the development of this science and the evolution of the practical problems posed by the increasingly demanding technological applications. As an example, the development of railroad transportation, combustion engines, and the introduction of steel as structural material brought many new problems dealing with strength of structures. Indeed, it was discovered that subjecting a metallic material to many cycles of stresses can produce fracture, by much smaller forces than would be required for static failure [Morin 1853]. This began the investigation of fatigue failure in iron, which initially aimed

at estimating how frequently locomotives had to be inspected and maintained in order to prevent fracture. To this aim, experiments applying a cyclic deformation to iron beams were performed (Fig. 1.4a), and the development of plasticity under finite strains was addressed, in connection with the onset of irreversibility of the macroscopic deformation [Fairbairn 1864]. At the same time, the microscopic origin of fatigue was investigated, but no consensus could be reached only based on macroscopic experiments. For this reason, in 1850 came the first suggestion of coupling fatigue test and microscopic investigation, from P.R. Hodge: *"To arrive at any true results as to the structure of iron it would be necessary to call in the aid of the microscope, to examine the fibrous and crystalline structure"* [Engineers 1851]. At the time such coupling was technologically out of reach, so that the change in iron microstructure had to be investigated separately. This limitation, coupled to the low sensitivity of existing imaging apparatuses, was such that no relevant observation could be made, yielding the conclusion that no real difference could be perceived between the sample before and after the fatigue treatment.

One has to wait almost one century before the first pioneering attempt, by G.I. Taylor [Taylor 1934], of coupling macroscopic deformation to a simultaneous measurement of microscopic structure and dynamics, with the aim of characterizing the destabilization and rupture of "highly viscous" drops under large deformations. To achieve this, a fixed stress was applied by controlling the deformation rate of the surrounding medium (Fig. 1.4c-d), while an imaging system provided magnified picture of the drop under increasing stress conditions, up to its failure (Fig. 1.4e). Interestingly, the mechanical properties of the bulk materials were also tested, using a home-made instrument which can be considered the ancestor of our stress-controlled rheometers (Fig. 1.4b).

1.3 State of the art

1.3.1 Steady-rate experiments

Many different protocols are used in literature to probe yielding and failure in soft materials. Probably the most straightforward of those protocols is represented by steady-rate experiments, where the material, initially at rest, is deformed at a constant deformation rate. Such an experiment can be performed in different deformation geometries, from well-defined ones like shear [Costanzo 2016, Keshavarz 2017], extension [Costanzo 2016] and compression [Antonaglia 2014], to more complex ones, like indentation or bending. In the following, we will focus on shear deformation, whereas appendix B will show simulations and experiments in uniaxial extension.

In steady-shear rate experiments, the stress σ is measured as a function of time, starting from the moment where the deformation rate is applied. An initial linear regime is observed at small deformations, where the stress growth is dictated by the linear viscoelastic properties of the sample. Beyond the linear regime, σ depends on the imposed shear rate $\dot{\gamma}$, in a way that can be rationalized in terms of the ratio between the largest

(terminal) relaxation time τ of the system and the experimental timescale $\tau_{exp} \sim \dot{\gamma}^{-1}$. When the product $Wi = \dot{\gamma}\tau$ (the so-called Weissenberg number)[Dealy 2010]) is small ($Wi \ll 1$), the deformation can be thought as quasistatic: the system relaxes faster than it is sheared, and can be considered at equilibrium at any time during the deformation. In this case, no deviations from linear rheology are expected. By contrast, in the opposite limit of $Wi \gtrsim 1$, the sample has no time to relax during deformation, and eventually is driven out of the linear regime. The linear to nonlinear transition can manifest in qualitatively different forms: brittle materials break abruptly, almost without any plastic deformation, whereas ductile ones exhibit substantial large plastic deformations after yielding. Because plasticity dissipates elastic energy, ductile yielding is generally associated to a downturn in the measured stress: eventually, after a first strain hardening regime [Groot 1996, Gardel 2004, Storm 2005, Pouzot 2006], the stress passes through a maximum (defining the failure stress and strain) and decreases afterwards [Mohraz 2005, Kabla 2007, Skrzyszewska 2010, Keshavarz 2017]. The detailed microscopic processes associated to departure from linear viscoelasticity and plastic yielding can be complex [Koumakis 2011, Costanzo 2016], so that in general their investigation is challenging and can usefully be supported by numerical works. To highlight the main open questions in this field, hereafter we review a few experimental studies, with particular focus on network forming systems and physical gels.

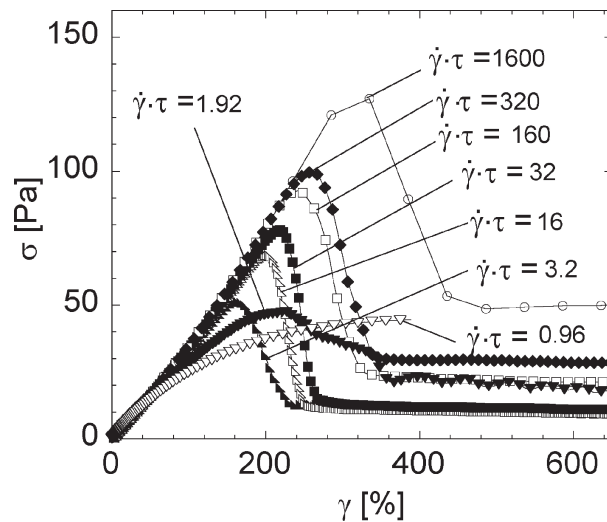


Figure 1.5: Protein physical gel. Time-resolved stress response as a function of strain ($\gamma = \dot{\gamma}t$) after start-up of steady shear. The reduced shear rates ($\dot{\gamma}\tau$) are indicated near the lines, with τ equal to 3200 s. Extracted from [Skrzyszewska 2010].

As a first example, working with a recombinant protein able to form supramolecular bonds with a well defined characteristic lifetime τ , Skrzyszewska *et al.* [Skrzyszewska 2010] show that a ductile to brittle transition is observed with increasing Weissenberg number beyond 1 (Fig. 1.5). The authors argue that at the lowest shear rates the stress deviates downwards because of the viscoelastic relaxation of the physical gel (associated to dis-

sociation and reformation of physical bonds), which leads to simple viscous flow in the steady state, whereas at larger shear rates this mechanism cannot happen anymore, and one observes instead a slight strain hardening, associated to the finite chain extensibility, followed by chain pull-out and brittle fracture.

In another work on a protein gel with no measurable terminal relaxation time, Keshavarz *et al.* observe brittle fracture for all values of $\dot{\gamma}$, since the condition $Wi \gg 1$ is always met [Keshavarz 2017]. Interestingly, the authors show that the whole stress-strain curve, up to the onset of mechanical instability, can be nicely predicted by a nonlinear viscoelastic model based on time-strain separation (Fig. 1.6). In this case, the departure from linearity can be accurately described in terms of a strain hardening and a strain softening term, and the deviation from the model is attributed to fracture. Indeed, thanks to direct visual inspection of the gel during deformation, the authors can detect the nucleation and growth of cracks, which appear at the yield point and are clearly associated to the subsequent stress drop. The authors argue that failure occurs as a consequence of stress-induced damage accumulation, which becomes critical beyond a given threshold. The rate of damage accumulation is assumed to be a function of stress alone, which provides an excellent prediction of failure stress and strain based on a failure criterion proposed by Bailey [Freeds 2002]. Therefore, one question that opens concerns the nature of the plastic rearrangements considered by Bailey's criterion. To elucidate this point, standard rheology might benefit from a microscopic investigation of the local structure and dynamics.

One example of such investigation can be found in the work of Mohraz and Solomon [Mohraz 2005], who study the structure of weak fractal colloidal gels subject to start-up of steady shear flow, by coupling shear rheology to time-resolved small angle light scattering. With increasing deformation, an anisotropic intensity pattern is detected in the light scattering signal, which signs a slight orientation in the gel structure [Vermant 2005]. The structural anisotropy initially increases as the gel is deformed, then reaches a maximum value at the yield strain (defined by the locus of the stress maximum) and afterwards decays to a plateau, in a qualitatively similar way to the macroscopic stress. Such similarity suggests that structural reorientation determines the nonlinear rheology of the gel. Moreover, by investigating the microscopic dynamics after flow cessation, the authors argue that minor connectivity loss should take place before the stress peak. It is interesting to compare this result to Bailey's criterion evoked by Keshavarz *et al.*, which rather suggests a more progressive weakening. The comparison is not trivial, and calls for a deeper understanding of the interplay between local plasticity and macroscopic rheology. On the other hand, both works agree in interpreting the stress drop as the macroscopic signature of gel rupture, which occurs abruptly at a large critical strain (around 100%), where the gel backbone should be fully extended. Accordingly, the rupture is associated to a maximum in structural anisotropy, and is followed by a partial relaxation of both stress and anisotropy, in a process read as the densification of fractal clusters.

More detailed insights on the microscopic processes occurring under shear are reported by Masschaele *et al.* [Masschaele 2009], who observe in real space the shear deformation

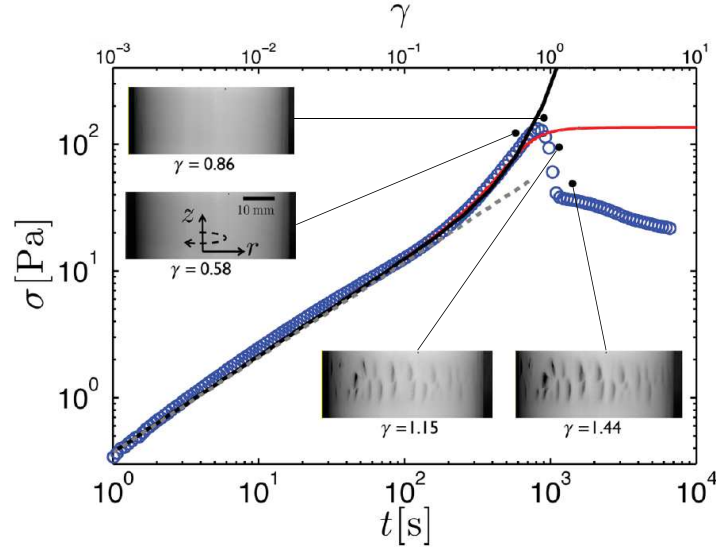


Figure 1.6: Protein gel. Stress response σ vs time t (lower axis) and vs strain $\gamma = \dot{\gamma}_0 t$ (upper axis) to a constant shear rate $\dot{\gamma}_0 = 10^{-3} \text{s}^{-1}$ initiated at $t = 0$. The gray dashed line corresponds to the linear viscoelastic response (a power law of time). The black line corresponds to the nonlinear model (K-BKZ) constructed using only the strain-hardening part of the damping function, whereas the red line corresponds to the full K-BKZ equation, which includes both the hardening and the softening components of the damping function. Insets: images of the side view of Couette cell at different strains recorded simultaneously to the experiment reported in the main graph. Adapted from [Keshavarz 2017].

and rupture of 2D fractal gels at oil-water interface. Unfortunately, the shear stress could not be measured in their experiments, so that the linear to nonlinear transition and gel rupture are only investigated at the microscopic scale. The authors rely on the assumption that the rheology of interfacial gels would show the same qualitative features as the analogous three dimensional structures. In agreement with Mohraz and Solomon, Masschaele *et al.* find that at small strains the gel network remains intact, and percolation is only lost at higher strains, where rupture occurs abruptly, as a consequence of a cascade of break-up events, which are monitored throughout deformation. Interestingly, break-up events are found to be spatially localized and tend to cluster, which might suggest some interesting correlations, neglected by the simple additivity of Bailey's criterion. In the regime of increasingly nonlinear deformation, the authors address various microscopic structural indicators in order to quantify the increased heterogeneity of the structure during deformation. Essentially all indicators show minor evolution prior to rupture, whereas the heterogeneity increases after rupture, in line with the findings of Mohraz and Solomon. Finally, the authors show that the pertinent lengthscale for breaking and structural reorganization coincides with the lengthscale of structural heterogeneity, i.e. the cluster size. More precisely, Fig. 1.7 shows an example of the typical plastic rear-

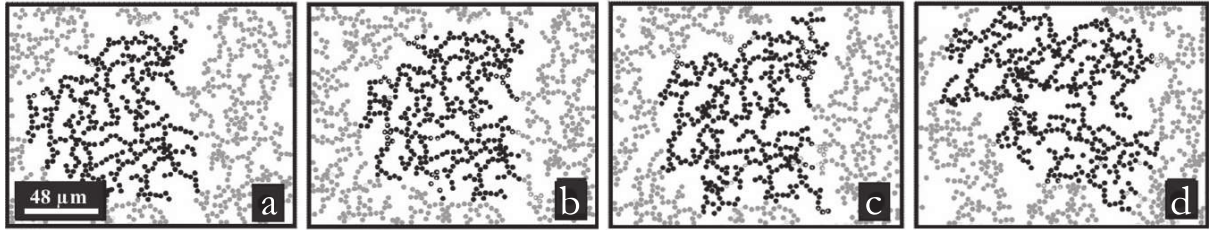


Figure 1.7: 2D colloidal gel: details of yielding of one particle cluster. The snapshots correspond to the network after a strain of, respectively, 0.25 (a), 0.5 (b), 0.75 (c), and 1.25 (d). Adapted from [Masschaele 2009].

rearrangement occurring at yielding: the bonds between clusters break, and as a consequence percolation is lost and groups of particles, which retain their integrity, are free to rotate collectively relative to the surroundings. This mechanism is in agreement with previous models for gel rupture, only based on rheological measurements [Shih 1990].

Many of the above results are corroborated and extended by numerical simulations, for which steady-rate experiments represent a particularly convenient framework. For example, the work of Park *et al.* [Park 2013, Park 2017] agrees on the observation of a structural anisotropy under shear, which reaches its maximum at yielding, whereas Boromand *et al.* [Boromand 2017] focus on bond distribution as an efficient way to characterize $\dot{\gamma}$ -dependent structural evolution during shear. In the same vein, Colombo and Del Gado [Colombo 2014] follow the bond breaking and reformation, emphasizing the relevance of bond orientation relative to shear. In agreement with Masschaele *et al.*, they show that bond breaking only starts occurring beyond 30% deformation, and that the onset of bond breaking is connected to the overstretching of the weakest chains, where the stress gets localized. Interestingly, the authors also discuss the microscopic reversibility of the deformation, by inverting the shear direction after reaching a given strain γ_{inv} and bringing back the system to the initial $\gamma = 0$ state. A comparison between the system at the beginning and at the end of this strain cycle shows that irreversible nonaffine displacements start to occur around $\gamma_{inv} \approx 10\%$, significantly before the onset of bond breaking.

In conclusion, we learn from steady-shear rate experiments that the yielding of network forming systems such as physical gels can occur in a brittle-like fashion under specific conditions. Brittle rupture is associated with a sudden drop of the measured stress, which is caused by a cascade of break-up events weakening the stress-bearing backbone of the network and triggering mechanical instability. This occurs at a characteristic lengthscale equal to the network mesh size, which for a colloidal gel corresponds to the size of the fractal cluster. During the deformation precluding rupture, such materials exhibit minor structural rearrangement, and the network connectivity is mostly preserved. At the same time, strain hardening is observed in the mechanical response, and it is associated to the orientation of the gel network in the shear direction.

A question that remains to a large extent open concerns the amount of bond breaking

events occurring during the deformation, and their eventual space and time correlations. If no bond breaking at all is expected in the linear regime, it is likely that, as it is observed by Masschaele *et al.* and in computer simulations, some bonds will break during nonlinear deformation. The amount of those breaking events, their nature and their relevance for the observed mechanical properties are usefully disclosed by simulations, but experiments are still blind to such information, which is presumably sample- and experimental-protocol dependent. A first indication can be obtained thanks to the models accounting for the macroscopic rheology. For instance, the applicability of durability criteria to model the onset of mechanical instability discussed by Keshavarz *et al.* seems to suggest that in some cases plasticity should occur throughout the deformation, at a well defined and stress-dependent rate (thus precluding avalanche-like dynamics as observed for some other systems [Antonaglia 2014, Kurokawa 2015]). The impressive agreement between the nonlinear model and the experimental data encourages deeper investigation on its microscopic implications: in this perspective, it was shown with the above examples that novel experiments accessing at the same time the mechanical response and the microscopic structure and dynamics tremendously increase our insight in the material behavior.

1.3.2 Creep experiments

Because of the rather robust rheological features observed and the well-defined experiment duration, steady-rate experiments are particularly convenient to study yielding. This explains their widespread application since Leonardo's ancient times [Timoshenko 1953]. The main disadvantage of this technique is perhaps that the shear history imposed to the sample is usually quite distant from the one typically experienced by materials in real life applications. For example, as mentioned above, snow avalanches, rockslides and sandslides occur under the constant force exerted by gravity, which may also cause the delayed collapse of civil structures like buildings and bridges as well as soft materials, whereas earthquakes and volcano eruptions are triggered by a nearly-constant stress due to the underground activity of earth's inner layers. On a smaller scale, failure of cables, fibers or adhesives usually occurs as well under a controlled stress. The latter case is particularly frequent, as it is well known to those who have tried to fix a post-it, a poster or a picture to a vertical surface with the help of an adhesive tape. Those people might have noticed with great disappointment that, despite its apparent initial stability, their creation had a limited lifetime, and it would eventually collapse after a while. The above examples push to address material failure with a second experimental protocol, where the sample is subject to a constant load and its deformation is monitored over time until delayed failure it eventually observed. Because the material is often observed in these experiments to progressively weaken, the term *fatigue* is sometimes used. In particular, when the external load is constant, one speaks about static fatigue (or creep), as opposed to dynamic fatigue, which is typically probed under cyclic stress or strain

[Poncelet 1839].

There is also a second, more fundamental reason for considering static fatigue of materials. Namely, in most of the models introduced in the literature, failure is regarded at the microscopic scale as a stress-controlled phenomenon. Remarkable examples include the Eyring model [Eyring 1936], the original fiber bundle model [Daniels 1945] and many of its derivations [Pradhan 2005, Kun 2003, Jagla 2011]. For this reason, a straightforward comparison between the various models' predictions and experimental results obtained in steady-rate is sometimes difficult to obtain, whereas static fatigue represents a much more natural framework.

1.3.2a Linear and nonlinear creep

The main disadvantage of static fatigue experiments is that sample deformation is not controlled. As a consequence, the duration of the experiments is often long and difficult to predict, sometimes because of experimental reasons like sample to sample variations and uncertainties on the applied stress, and sometimes for more fundamental reasons, like the intrinsically stochastic nature of fracture nucleation and growth [Griffith 1921, Weibull 1939, Bonn 1998]. During the potentially very long induction times, which on structural materials can extend to several years [Maekawa 2016], the effect of fatigue is observed at the macroscopic scale as a slow deformation called creep, which is usually well described either by a logarithm of time [Phillips 1905, Nabarro 2001, Nechad 2005b, Siebenbürger 2012], by a power law [Andrade 1910, Plazek 1960, Caton 2008, Rosti 2010, Grenard 2014, Leocmach 2014, Koivisto 2016, Ballesta 2016], or by combinations of the two [Wyatt 1951, Cherièr 1997, Siebenbürger 2012].

A major fundamental issue related to creep is to understand the underlying microscopic processes responsible for the observed sublinear deformation. If this is rather understood in crystalline materials [Poirier 1985] like metals [Andrade 1910, Miguel 2002, Cottrell 1952] or ice [Ashby 1985] in terms of defect motion, for amorphous materials the problem is complicated by the fact that structural defects are not as well defined [Widmer-Cooper 2009, Schoenholz 2014]. In particular, amorphous materials are often viscoelastic, thus a time-dependent response may arise as well as a simple consequence of linear viscoelasticity, in absence of damage or plastic events. Decoupling the two contributions is generally far from trivial, all the more since several models, based on radically different assumptions, from pure linear viscoelasticity [Mainardi 2010, Hilfer 2000, Friedrich 1991, Heymans 1994], to pure plasticity [Pradhan 2005, Eyring 1936, Zapperi 2000, Bocquet 2009], to a combination of both [Kun 2003, Jagla 2011], can equally account for the observed macroscopic deformation.

In general, in the limit of small applied stresses, and consequently small deformations, creep is linear viscoelastic: the measured deformation can be described in terms of a linear creep compliance, which can be compared with independent measurements in the linear regime, say in the frequency domain [Evans 2009]. This can be exploited in order to

probe linear viscoelastic processes occurring on timescales too long to be characterized by oscillatory rheology (cf. chapter 5). Upon increasing the applied stress, however, an additional contribution to structural relaxation is introduced by emerging nonlinear processes, which lead to faster (shear thinning) flow in the steady state observed in the long time limit [Erwin 2010].

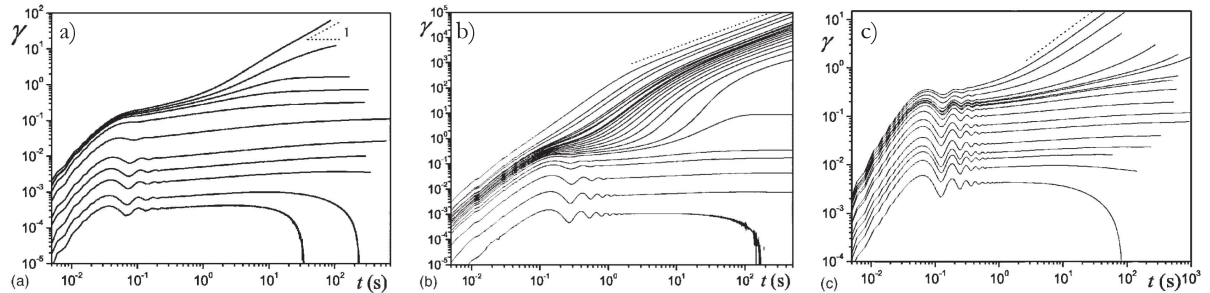


Figure 1.8: Typical aspect of deformation vs time curves for different stress levels σ (increasing from bottom to top) applied to the following soft-jammed systems: (a) Mustard, (b) Bentonite suspension, (c) Hair gel. The inclined dotted line is the curve of slope 1. Adapted from [Coussot 2006].

This is discussed in detail by Coussot *et al.* [Coussot 2006], who introduce the concept of viscosity bifurcation to explain the experimental observation that for a small increase in the applied stress σ from below to above a given threshold σ_y (the so-called yield stress) the steady-state shear rate increases from zero in the solid regime ($\sigma < \sigma_y$) to a finite value, apparently larger than a critical strain rate $\dot{\gamma}_c$ (Fig. 1.8). This phenomenon appears to apply quite generally to a class of yield stress fluids which are called thixotropic. However, from Fig. 1.8 it is clear that the steady state is not reached instantaneously and that transient regimes, e.g. separating solidlike behavior at rest from liquidlike behavior beyond yielding, convey tremendous physical information on the yielding process. In particular, Coussot *et al.* remark that in some cases, close to the yield stress, the induction time can exceed the experiment duration, and that in those cases it is difficult to say whether the material will ultimately stop or reach a steady flow over very long times.

The transient creep deformation before fluidization is addressed for example in the work of Siebenbürger *et al.* on colloidal glasses [Siebenbürger 2012]. Their data (Fig. 1.9) show distinct regimes: (i) an initial transient, dominated by the coupling between sample viscoelasticity and inertia of the measurement tool (called creep ringing [Ewoldt 2015]), is followed by (ii) a first linear viscoelastic response, which corresponds to a quasi-plateau in the measured deformation. Later on, plastic deformation is observed, and takes different forms according to the applied stress σ . At large σ , a steady state characterized by viscoplastic flow (iii) is reached after a superlinear deformation regime (iv), whereas at low σ sublinear creep continues indefinitely (v): creep appears to be logarithmic in the long time limit, but before that a power-law transient is also found, whose duration may extend to nearly one week depending on sample age. Whereas no real explanation is given

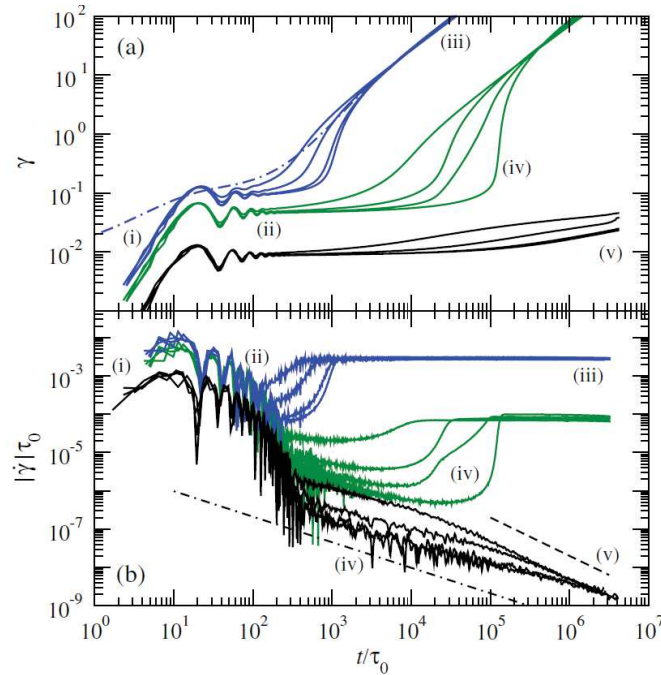


Figure 1.9: Colloidal glass. (a) Deformation $\gamma(t)$ for increasing applied stress (different colors from bottom to top), and increasing waiting times after shear-induced rejuvenation (for each color, increasing from left to right). Time is rescaled using the diffusion time $\tau_0 = R^2/D_0 = 4\text{ms}$ (R being the particle radius and D_0 being the free diffusion coefficient). The different regimes described in text are marked with roman labels (i)-(v). (b) Associated normalized shear rate $\dot{\gamma}(t)\tau_0$. Dash-dotted line: Andrade creep law, $\dot{\gamma}(t) \sim t^{-2/3}$; dashed: logarithmic creep, $\dot{\gamma}(t) \sim 1/t$. Extracted from [Siebenbürger 2012].

for the transient power law creep, the authors propose a nonlinear model accounting for the logarithmic creep, based on the assumption that the nonlinear relaxation modulus is described by a nonlinear generalized Maxwell model [Voigtmann 2011], whose essential ingredient is that in the high shear rate limit the material displays shear thinning as a simple yield stress fluid ($\eta \propto \dot{\gamma}^{-1}$). Other models can be found in literature, relating the logarithmic creep to more microscopic quantities like the activation energy for plastic rearrangements. Nabarro reviews two of them, the work-hardening model and the exhaustion model [Nabarro 2001]. These models were developed to describe the deformation of granular materials, and are essentially elasto-plastic, with no account for linear viscoelastic deformation. Without entering into details, we observe that the amount of different models existent in literature and producing identical predictions for the rheology should be regarded as an indication that it may be hard to get a true microscopic insight from macroscopic measurements alone.

In this regard, an instructive example is discussed by Chérieire *et al.*, for the torsional creep of PMMA, a polymer glass [Cheriere 1997]: at low temperatures a simple logarithmic creep is observed, but as temperature is increased the first logarithmic creep regime

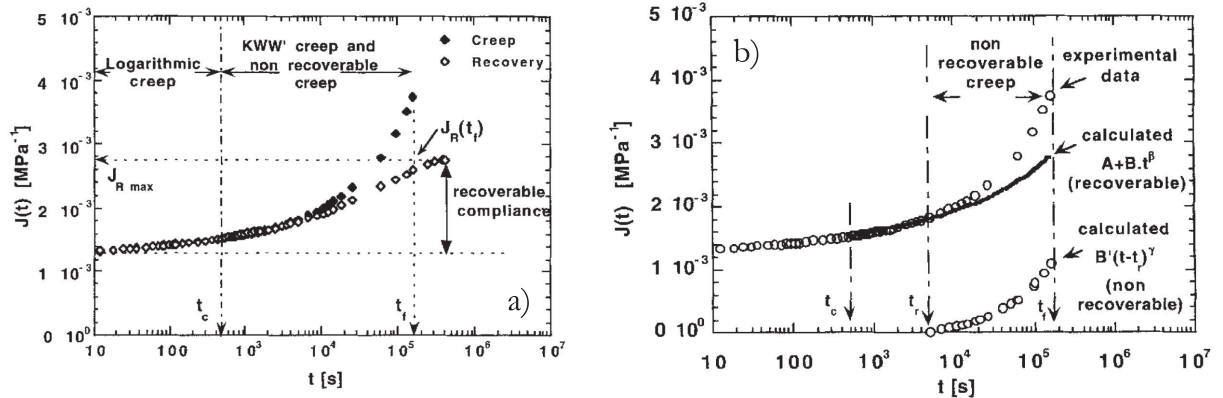


Figure 1.10: Polymer glass. (a) Experimental creep and recovery at 90°C . Creep is partly recoverable. The magnitude of the recoverable creep is $J_{R,max}$; this allows determination of the maximal compliance $J_R(t_f)$ reached by the recoverable creep at $t = t_f$. (b) Beyond of the end of the logarithmic creep, $t_c = 500$ s, analysis of the experimental creep curve obtained by addition of two creep contributions: a recoverable creep deduced creep recovery and a nonrecoverable creep obtained by difference from the total creep. Extracted from [Cheriere 1997].

is eventually followed by a power-law regime. At still higher temperatures, approaching the glass transition from below, a third regime follows, described by a different power law. This is analogous to the behavior of many metals [Wyatt 1951]. The originality of the work of Chérière *et al.* consists in a thorough discussion of the recoverability of creep deformation, which is probed by releasing the applied stress after a given time and by following the relaxation of the strain. If the stress is released during the logarithmic creep, the authors observe a logarithmic strain recovery, which completely recovers the initial zero-deformation state after a time equal to the time spent under stress. Complete recovery is also found when the stress is released during the first power-law creep, but in this case the recovery process takes longer than the creep time. Finally, the second power law creep is only partially recovered. The complete picture is represented in Fig. 1.10. Such observation about macroscopic reversibility is very interesting, because it is contrary to the intuitive notion of creep as presented by the previous works. In those works, creep was regarded as the result of a series of irreversible structural rearrangements, which should leave behind them no or minor driving force for recovering the unstrained state once the macroscopic stress is released. Here, by contrast, the authors correctly point out that plasticity might be reversible, as long as the main stress bearing structure is not damaged: in that case, upon stress release, the system will maintain the tendency of recovering its initial rest state. Moreover, this also explains why recovery is also a gradual processes, since it can attain completion only after a number of plastic rearrangements comparable with the ones that occurred during creep, which explains the symmetry between the two processes as observed by rheology. Following this line of thought, the authors speculate

that entanglements start to be lost only during the third regime, which is only partially recovered.

The potential recoverability of creep is conceptually intriguing and hides a subtle distinction between recoverability of macroscopic strain and reversibility of the single microscopic processes occurring under creep. For example, one may wonder whether the final state after complete strain recovery corresponds to the same microscopic configuration as the one before stress application. In this regard, such a distinction is strongly related with the key questions mentioned above, and deserves deeper investigation. In particular, Fig. 1.10b reveals a rather well defined transition between fully recoverable and only partially recoverable creep. From that same figure, it is clear that a clear distinction between the two regimes can hardly come from an observation of the shape of the creep curve, and that complementary observations may be usefully coupled to the macroscopic rheology.

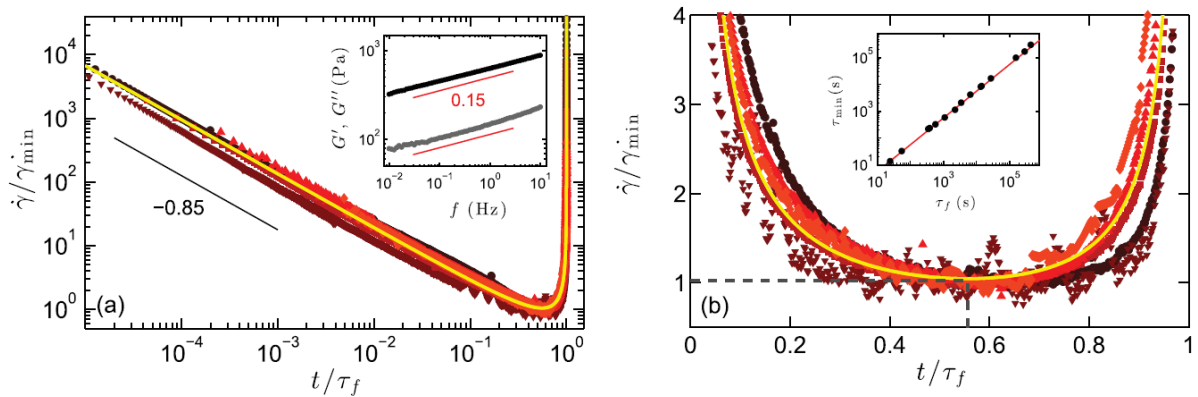


Figure 1.11: Protein gel. (a) Normalized shear-rate responses $\dot{\gamma}(t)/\dot{\gamma}_{min}$ for different values of the applied stress and plotted as a function of the rescaled time t/τ_f , where τ_f is the failure time and $\dot{\gamma}_{min}$ is the minimum shear rate reached at τ_{min} . Inset: Linear viscoelastic moduli G' (top) and G'' (bottom) as a function of frequency f for a strain amplitude of 0.1%. Red lines are power laws $G' \propto G'' \propto f^{0.15}$. (b) Same data as in (a), but with the time axis in linear scale to emphasize the secondary creep. Inset: τ_{min} vs τ_f . The red line is $\tau_{min} = 0.556\tau_f$. Extracted from [Leocmach 2014].

Fully recoverable creep was also found by Leocmach *et al.* on a completely different system, namely a protein gel [Leocmach 2014]. In this case, the creep deformation is characterized by three regimes (Fig. 1.11), with a first power-law creep (called primary creep), which, under large enough stresses, is followed by a secondary creep characterized by an upward deviation from the power law, with a minimum in the deformation rate, and finally a tertiary creep, where the deformation accelerates, exhibiting an ideal power-law divergence at a finite time t_f where macroscopic failure is observed. The authors find that the power law characterizing primary creep corresponds to the linear creep compliance as it can be inferred by independent measurements (Fig. 1.11a, inset). This rules out

most of the mechanisms invoked by the above works, where significant creep was only observed under large enough stresses (cf. Fig. 1.8), and calls for a linear deformation mechanism, perhaps inspired by the rheology of critical polymer gels, which also display extended power laws as a consequence of their fractal structure [Adolf 1990]. As a further confirmation for linearity, the authors perform a series of creep and recovery tests, each time finding a complete recovery, which suggests that no or minor damage is cumulated by the material during primary creep. Thus, very interestingly, the authors point out that the onset of secondary creep in the rheological signal corresponds at a more fundamental level to the onset of irreversible processes, which introduce an additional contribution to the macroscopic deformation, eventually becoming predominant during the tertiary creep. Thus, a clear detection of such transition holds the promise of providing a means of predicting the failure time t_f before the material is excessively damaged, which is a problem of fundamental practical interest. The authors point out that an analysis of the shape of the $\dot{\gamma}(t)$ curves might allow such prediction. Indeed, as it is shown in Fig. 1.11b, in every experiment $\dot{\gamma}$ exhibits a minimum at a time t_m simply related to t_f by a linear relation (Fig. 1.11b, inset): a measurement of t_m would yield a straightforward prediction of the failure time t_f .

An analogous linear relation (first determined by Monkman and Grant in 1956 [Monkman 1956]) is also found on composite materials under tensile creep [Nechad 2005b, Rosti 2010, Koivisto 2016]. In particular, Koivisto *et al.* explicitly discuss the possibility of achieving a robust failure prediction based on the detection of t_m [Koivisto 2016]. They show that despite both t_m and t_f individually suffer huge sample to sample variations, the ratio t_f/t_m is very well defined (and equal to 0.83 in their case, whereas it is 0.556 for Leocmach *et al.*), and it thus represents a very robust and reliable indicator. However, the authors also remark that the experimental measurement of t_m is in practice very delicate, because of both experimental noise and intrinsic fluctuations, and they conclude that such a method for predicting t_f would not be practical. In conclusion, the authors identify two main challenges associated to creep failure time prediction: the first one is to find some physical quantity measurable during the first stages of the creep and displaying strong correlations with the failure time, and the second is to properly measure it, recognizing precursory features as such. These are the same challenges faced by the attempts to predict earthquakes: although foreshocks clearly do exist, the main problem is detecting them on time and recognizing them in their precursory nature [McGuire 2005].

Therefore, it appears that also the effort of predicting delayed failure could largely benefit from a more microscopic insight, where the smooth transition from sublinear primary creep to accelerated tertiary creep observed in rheology might be sharper and easier to detect.

1.3.2b Microscopic dynamics during creep

An insight on microscopic plasticity can be obtained in some cases by recording the crackling noise emitted by the sample under creep. Indeed, many systems under creep

emit a characteristic intermittent noise called crackling, which has been linked to sudden, collective plastic events occurring at the microscopic scale [Myers 2001]. Known since long time in the framework of earthquakes [Ben-Zion 2008] and snow avalanches [Sommerfeld 1983, Van Herwijnen 2011b, Van Herwijnen 2011a], it first entered the framework of material science through an investigation on crumpling paper [Houle 1996], and was thereafter detected on a variety of other systems, from metals [Antonaglia 2014, Abobaker 2015] and ice [Duval 2010, Gudipati 2012] to rocks [Agioutantis 2016], wood [Guarino 2002] and composite materials [Nechad 2005a, Nechad 2005b], including examples relevant to soft matter such as granular materials [Johnson 2013, Amon 2013] or foams [Tewari 1999, Kabla 2007]. The statistical properties of crackling were shown to follow characteristic power-law size distributions, and even the detailed shape of the temporal evolution of one single event was shown to be universal [Antonaglia 2014], and common to a wide class of completely different phenomena, from solar flares [Lu 1993] to fluctuations in the stock market [Bak 1997], with many other examples reviewed by Myers *et al.* [Myers 2001]. This result has been read as an indication that creep and yielding could be described in a sample-independent fashion, and studied in the larger framework of nonequilibrium phase transitions [Hinrichsen 2000], and as such it has whipped up enthusiasm in the scientific community. For this reason, the shape and the statistical properties of crackling noise have been addressed in several analytical [Papanikolaou 2011, Dahmen 2011] and numerical works [Durian 1997, Carmen Miguel 2001, Pradhan 2005, Tsamados 2010, Jaiswal 2016, Bouzid 2017], and concepts borrowed from this field were used to interpret macroscopic stress fluctuations observed in experiments [Antonaglia 2014, Kurokawa 2015].

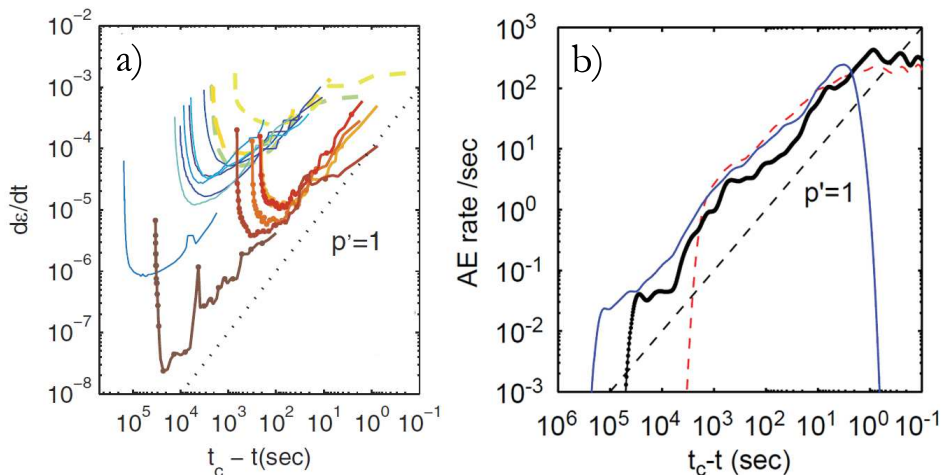


Figure 1.12: Ply glass / polyester composites. (a) Creep strain rate measured for 15 samples, plotted as a function of $t_c - t$ to emphasize the power-law divergence during tertiary creep (adapted from [Nechad 2005b]). (b) Rate of AE events for three representative samples plotted against $t_c - t$ (adapted from [Nechad 2005a]). In both plots, dashed lines correspond to the law $1/(t_c - t)$.

For instance, a remarkable experimental observation has been obtained for the delayed creep failure of composite materials [Nechad 2005a, Nechad 2005b]. Nechad *et al.* show that power laws govern the rate of acoustic emissions (AE) during both primary and tertiary creep, in nice qualitative agreement with the evolution of the macroscopic strain rate (Fig. 1.12). The authors use this observation to attribute the observed deformation entirely to microscopic plastic events (associated to crackling), since the very beginning of the experiment. This idea is supported by a theoretical model based on a modification of the fiber bundle model (FBM) [Pradhan 2010], complemented with ad-hoc viscoplasticity attributed to each fiber in order to reproduce correctly the complete creep curves. Despite the qualitative agreement between the measured $\dot{\gamma}$ and the numerical predictions, the model proposed by Nechad *et al.* suffers a few limitations, as pointed out by Jagla [Jagla 2011], the major defect being the fact that fiber ruptures in their modified FBM happen independently from each other, without any mechanism able to produce collective phenomena such as the microscopic avalanches associated to AE signal. Moreover, the nonlinear rheology attributed to each fiber (or representative element, in the language of Nechad *et al.*) is somehow artificial: both aspects leave the impression that the model proposed is too much coarse grained, and it does not grasp the fundamental dynamics actually occurring at the microscopic scale. Interestingly, it is shown by Jagla that other modifications of the original FBM, based on radically different assumptions, are also able to reproduce the $\dot{\gamma}(t)$ measured by Nechad *et al.*, and that some of these alternative solutions exhibit linear viscoelasticity and collective phenomena, both aspects missing in the original version. Once again, it appears that various models, profoundly different in essence, can nearly equally account for the same rheological features. Thus, if on the one hand AE data are very instructive, indicating the presence of plastic events with well defined statistical features, on the other hand their interpretation in terms of microscopic dynamics is not straightforward. Among the several questions that may arise, it is unclear for example if and how it might be possible to quantify the entity of the microscopic rearrangements producing one AE event, whereas the nature of the microscopic rearrangement is most probably not accessible with this technique.

Studying the tensile creep of paper, another composite displaying the same three creep regimes as the samples just discussed, Alava and coworkers resort to a more straightforward mesoscopic investigation, studying the evolution of spatial fluctuations in the local tensile strain as a way of addressing local plasticity and stress concentration [Rosti 2010, Koivisto 2016]. By coupling tensile creep and digital image correlation (DIC), the authors find that spatial fluctuations of local strain exhibit power-law scaling in time, indicating that power-law creep (also called Andrade creep regime) can be understood in terms on a nonequilibrium phase transition between "jammed" immobile states and "flowing", active states [Rosti 2010]. Moreover, the authors find a correlation between the amplitude of spatial fluctuations and the failure time, which is intriguing in itself, although again they conclude that this approach has only a limited benefit for the prediction of the failure time t_f [Koivisto 2016].

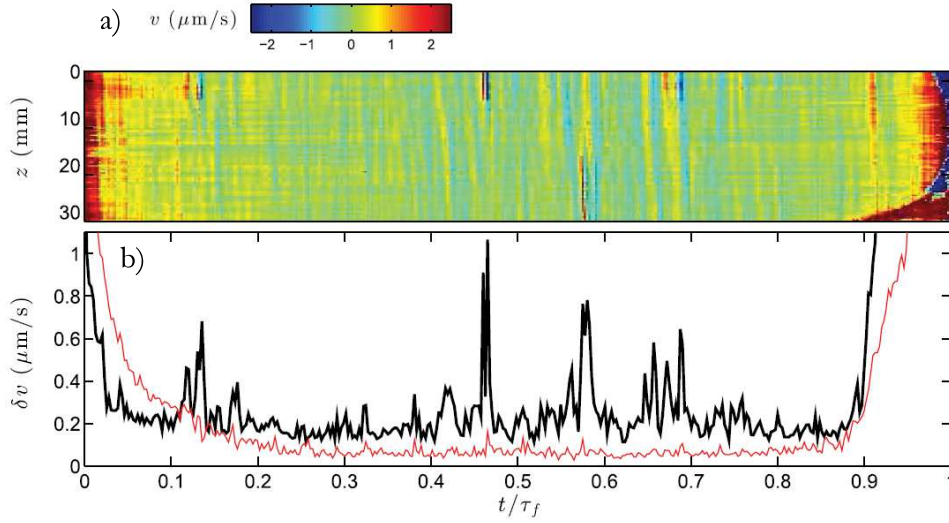


Figure 1.13: Protein gel. (a) Spatiotemporal diagram of the local velocity $\langle v(r, z, t) \rangle_r$ in the shear direction, averaged over the radial direction r and plotted in linear color levels as a function of z (coordinate in the vorticity direction) and t/τ_f (τ_f being the time to failure). (b) Standard deviation $\delta_z v(t)$ of $\langle v(r, z, t) \rangle_r$ taken over the vertical direction z (thick black line) together with corresponding standard deviation $\delta_r v(t)$ computed over the radial direction r on the z averaged $\langle v(r, z, t) \rangle_z$ (thin red line). Adapted from [Leocmach 2014].

Hence, the analysis of spatial heterogeneities in the local strain field appears to be a promising tool to achieve a better understanding of delayed creep failure. A very sensitive and practical probe for such heterogeneities has been developed by Manneville and coworkers, who in a long series of papers starting in 2004 [Salmon 2004, Manneville 2004] and continuing nowadays [Saint-Michel 2017] study the local velocity profiles with a novel ultrasound velocimetry technique. In an already mentioned example, Leocmach *et al.* apply this technique to the study of the creep and fracture of a model protein gel [Leocmach 2014], in order to elucidate in deeper detail the microscopic origin of the deviation from the linear viscoelastic primary creep. This is particularly intriguing since the authors show that the macroscopic $\dot{\gamma}(t)$ curve can be nicely described by the simple sum of a power law decrease $\sim t^{-\alpha}$, accounting for the primary creep, and a power law acceleration $\sim (t_f - t)^{-1}$, accounting for the tertiary creep (Fig. 1.11). Mathematically, this corresponds to a very smooth and gradual transition, implying that in fact plastic damage should occur throughout the experiment, even though it becomes macroscopically relevant only starting from the secondary creep. As a consequence of its gradual nature, this transition appears to be very elusive to macroscopic rheology. For this reason, the authors complement their study with a direct space investigation of strain heterogeneities, finding two interesting features: first, they observe the early nucleation, during secondary creep, of mesoscopic crack patterns, which grow in a subcritical way during tertiary creep,

a feature routinely observed in mechanical fatigue tests [Tomkins 1981]. They also show that the crack growth rate is proportional to the macroscopic shear rate, which sets the basis for a microscopic interpretation of the plastic deformation close to failure. Second, in stark contrast with the smooth rheology, the authors find that cracks nucleate in a discontinuous, intermittent way, which can be well characterized by space resolved ultrasound velocimetry (Fig. 1.13). In particular, the authors observe that the spatial fluctuations of the local velocities, quantified by their standard deviation δv (Fig. 1.13b), exhibit sharp peaks during the secondary creep, which are attributed to sudden plastic events like crack nucleation or intermittent growth. This suggests that the smooth evolution of the deformation observed in rheology is actually the result of an intriguing intermittent plastic dynamics occurring at the micro/mesoscopic scale, potentially showing common features with the crackling paradigm discussed above. This again demonstrates that a microscopic insight into the microscopic details of the dynamics under shear could provide a handy means of detecting the growing damage, which is a crucial parameter to get a better understanding and control on fatigue and delayed failure.

In this perspective, other scattering methods (different from ultrasound) can be coupled to shear rheology, namely light scattering, either in the single [Mohraz 2005] or in the multiple scattering regime [Ballesta 2016], X-ray scattering, either static [Denisov 2015] or dynamic [Leheny 2015], and neutron scattering [Kim 2014]. However, the already mentioned challenge of extracting the signal due to plasticity from the background given by affine deformation makes this technique more easily employed in oscillatory shear, as we will see in a while, whereas in transient experiments the use of scattering techniques is infrequent and limited to static scattering, which focuses on simple features like structural orientation [Mohraz 2005].

The most commonly employed technique to characterize the microscopic structure and dynamics under shear is microscopy. In particular, confocal microscopy has been widely used thanks to the possibility of accessing a full 3D information, essential to detect localized deformations, shear bands and complex microscopic rearrangements involving out-of-plane particle motion. The challenge faced by microscopy is again related to the already mentioned problem of averaging measurements on a statistically relevant ensemble, which typically limits the application of these techniques to the study of steady states, mostly in steady-rate experiments, where statistics can be improved by averaging over time. Nevertheless, there are a few fairly recent exceptions trying to investigate transient creep. For instance, Chan and Mohraz [Chan 2014] compare the microscopic dynamics under creep of a colloidal glass and a colloidal gel, and they observe that, despite their similar rheological behavior, the two systems exhibit rather different microscopic dynamics upon yielding. In particular, the dynamics observed in the gel accelerate abruptly when yielding occurs, whereas in the colloidal glass this transition is more gradual. The strong limitation of this work is that again, presumably because of poor statistics, the authors perform long time averages, which a priori is not justified in a transient experiment such as creep.

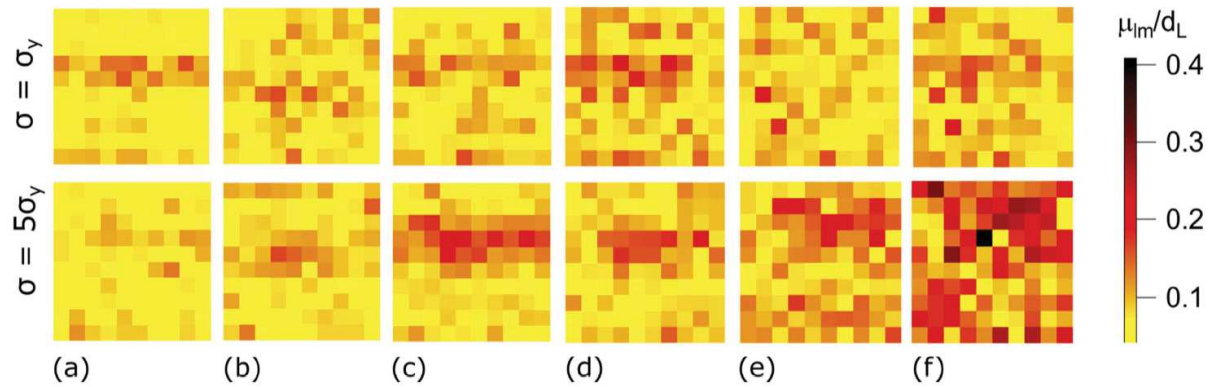


Figure 1.14: Binary colloidal glass. Maps of average particle mobilities $\mu_{lm}(t)$ normalized by the diameter d_L of large particles in the binary glass. Two different stresses are shown, one close to the yield stress ($\sigma \approx \sigma_y$, top) and a larger one ($\sigma \approx 5\sigma_y$, bottom). Different images are taken at different times during creep deformation, increasing from (a) to (f). Extracted from [Sentjabrskaja 2015].

On the other hand, the full space and time dependence of the observed microscopic dynamics is addressed with confocal microscopy under creep on a colloidal glass by Sentjabrskaja *et al.* [Sentjabrskaja 2015], in the attempt of characterizing the dynamics occurring prior to the delayed onset of flow. The authors measure the particles' mean square displacement Δy^2 along the vorticity direction (thus removing all contributions coming from the affine deformation), and observe a quantitative relation between Δy^2 and the macroscopic strain, indicating once again that creep deformation is a simple consequence of the plasticity that develops after the initial linear regime, as also suggested by a comparison with numerical simulations. An intriguing feature emerging from this work is that the onset of flow is associated to an increase of spatial heterogeneity in the plastic activity, with the appearance of regions of high local mobility and super-diffusive dynamics, whereas below the yield stress such heterogeneities remain almost constant in time (Fig. 1.14).

These examples show that the investigation of the slow dynamics occurring during sublinear creep is very challenging, but it is also crucial in order to achieve a better understanding, and possibly a prediction, of delayed creep failure. This is specially interesting since it could provide a means to monitor the health of a structure prior to its collapse. Some works pointed out that macroscopic indicators might exist [Nechad 2005b, Leocmach 2014], although their detectability is arguable [Rosti 2010, Koivisto 2016], whereas interesting dynamics are observed at a more local scale [Nechad 2005b, Leocmach 2014, Rosti 2010, Koivisto 2016, Sentjabrskaja 2015], potentially exploitable for predictions.

Clean experiments accessing at the same time the macroscopic creep deformation and the microscopic dynamics are very scarce, thus the microscopic origin of creep is far from being understood. Nevertheless, a few experimental works suggest the existence of a general framework, potentially able to describe creep and yielding without relying on the

specific details of the sample investigated.

One crucial step forward in this direction is therefore to identify the nature of the microscopic activity observed in the experiments, with particular focus on distinguishing reversible from irreversible processes. This is particularly challenging in transient experiments such as the ones discussed so far, and for this reason creep and steady-rate experiments are usefully complemented with measurements under a periodic stress or strain, where irreversible processes emerge as the only contributions to microscopic rearrangements observed across one or several periods.

1.3.3 Dynamic fatigue test

1.3.3a Reversibility and yielding in oscillatory shear

Thanks to the particularly simple mechanical response in the linear regime, oscillatory shear has been widely used to characterize the viscoelastic response of soft materials. By contrast, the mechanical response becomes generally very complex in the nonlinear regime, and sophisticated analysis is required to obtain a consistent picture [Rogers 2011]. Despite its complexity, it turns out that large amplitude oscillatory shear (LAOS) provides access to amazingly detailed information on the microscopic processes occurring during deformation, and much can be learned by such experiments [Hyun 2011].

As an example, we consider here the work of Carrier and Petekidis on the nonlinear rheology of a model soft colloidal glass [Carrier 2009]. The two main results of this work are summarized in Fig. 1.15: the first-harmonic viscoelastic moduli plotted as a function of the strain amplitude γ exhibit a trend similar to the one of Fig. 1.2, with a linear regime at small γ , a concentration-dependent yielding transition with a characteristic peak of G'' and a terminal regime in the limit of large amplitudes. A Fourier analysis of the detailed shape of the stress response of the sample reveals the appearance of higher order harmonics at finite amplitudes, marking a linear to nonlinear transition which appears to be sharper and shifted at higher strains for denser samples (Fig. 1.15b).

To account for the observed phenomenology, the authors propose a model based on a modification of the fluidity model by Derec *et al.* [Derec 2003]. The main assumption of this model is that the structural relaxation rate τ^{-1} can be decomposed in the independent (additive) contribution of a spontaneous relaxation rate τ_0^{-1} and a nonlinear, shear-induced contribution, which is called fluidity and denoted with the letter D . The structural relaxation time τ is then employed in a Maxwell-type constitutive equation: $\dot{\sigma} = -(D + \tau_0^{-1})\sigma + G(D)\dot{\gamma}$, where the elastic modulus $G(D)$ of the Maxwell fluid is also dependent on shear. Thus, the mechanical response to an arbitrary shear history can be computed once the time evolution of the fluidity is described by a kinetic equation. The expression postulated by Derec and borrowed by Carrier and Petekidis is very general, and reads:

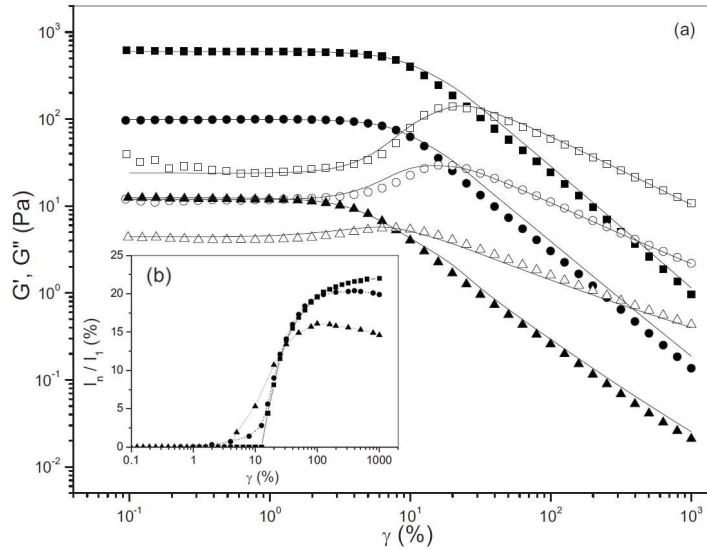


Figure 1.15: Soft colloidal glass. (a) Dynamic strain sweeps for three different volume fractions, decreasing from top ($\phi = 1.29$, squares) to bottom ($\phi = 0.77$, triangles). Experimental storage (closed symbol) and loss (open symbols) moduli. The model predictions are depicted with solid lines. (b) Fourier transform rheology: fraction of third harmonic versus strain amplitude for the same three volume fractions. Adapted from [Carrier 2009].

$$\dot{D} = \left[r + u \left(\frac{\sigma D}{\dot{\gamma}} \right)^\lambda \frac{\dot{\gamma}^{\nu-\varepsilon}}{D^\nu} \right] D^\alpha - v D^{\alpha+\beta} \quad (1.1)$$

where a set of 5 exponents ($\alpha, \beta, \lambda, \nu, \varepsilon$) and 3 coefficients (r, u, v) make the expression rather involved, so that even though experimental data are nicely described, it remains difficult to extract physical meaning from the model parameters. The relevant aspect of this work is that it links the measured nonlinear viscoelasticity to a conceptually simple microscopic quantity, which might be directly probed with techniques such as dynamic light scattering. Not only such measurements would represent a much stronger test of the fluidity model, but they could also provide a deeper insight on the nature of the microscopic processes responsible for the postulated strain dependence of the structural relaxation rate. More generally, a direct measurement of shear-induced structural relaxation would shed light on the microscopic origins of nonlinear rheology, which is one of the major fundamental open questions currently debated in the soft matter community [Schall 2007, Chan 2014], despite decades of attempts to find a general framework for these phenomena [Liu 1998, Trappe 2001].

To this aim, oscillatory rheology can be usefully coupled to more direct probes of the microscopic structure and dynamics. This is specially true since, although the linear and the large amplitude regimes are shared with similar features by all soft solids [Miyazaki 2006], the details of the yielding transition can be complex and reminiscent of the microscopic details of the sample, in particular for samples with a multiscale

structure such as star polymer glasses [Helgeson 2007] or colloidal gels [Koumakis 2011, Brunel 2016, Moghimi 2017]. Such a complex yielding calls for more direct methods to probe how the structure evolves under LAOS, and vice versa how yielding depends on the sample structure.

A first attempt at addressing these questions can be found in the work of Kim *et al.* [Kim 2014], who employ neutron scattering in order to study the structural modification of colloidal gels under large amplitude oscillatory shear. Focusing on the very large amplitude limit (γ_0 as large as 50 strain units), the authors observe that the large scale structure of the gel is periodically modified, which reflects in a periodic, anisotropic modulation of the scattered intensity at low scattering angles. This anisotropy is thoroughly characterized by the authors in both the velocity-gradient and the velocity-vorticity planes, and it is quantified by a structural parameter A_f employed in complicated 3D (σ, γ, A_f) diagrams inspired to the Lissajous plots (Kim *et al.* refer to those diagrams as structural Lissajous plots). We will see similar diagrams in chapter 7, where we argue that the concept of structural Lissajous plots has the potential to inspire and guide the delicate analysis of rheological Lissajous plots.

One limitation of neutron scattering, however, is the typically poor contrast, which limits the analysis to the highest strain amplitudes, preventing the authors from discussing the evolution of the structural signature across yielding. This problem is overcome by Schall and coworkers [Denisov 2015, Dang 2016] by employing synchrotron x-ray radiation on colloidal glasses. In this work, an anisotropy in the structure factor following strain amplitudes from the linear regime up to the large amplitude terminal regime is detected. In particular, the authors focus on tiny variations detected at a scattering vector corresponding to the position of the peak of the structure factor, where scattering techniques probe a lengthscale comparable to the distance between two particles in close contact. The authors argue that at such lengthscale the structural anisotropy stems from elastic shear distortion of the "cage" environment felt by each particle, which is also responsible for the elastic mechanical response observed in the linear regime (cage elasticity). Beyond the yield point, the observed response becomes prevalently liquid-like, a transition that is interpreted as shear-induced out-of-cage particle motion. Coherently, the authors find that the observed anisotropy vanishes beyond yielding. By introducing an ad-hoc order parameter, they measure the quadrupolar symmetry of the scattered intensity, and observe that it drops very sharply from 1 to 0 exactly in correspondence to the crossover between G' and G'' . They interpret this fact as the sign that cage elasticity is instantaneously and abruptly lost in a sharp transition reminiscent of thermodynamic first-order phase transitions. However, the authors admit that their interpretation is rather surprising, given the smooth crossover observed in rheology, and a true explanation of this apparent discrepancy is not proposed.

With the isolated (to the best of our knowledge) exception of this work, there is large consensus in the scientific community on the fact that the microscopic origin of yielding as it is observed in LAOS has to be attributed to a transition in the microscopic dynamics, rather than in the structure [Kawasaki 2015]. A convenient way of addressing irreversible

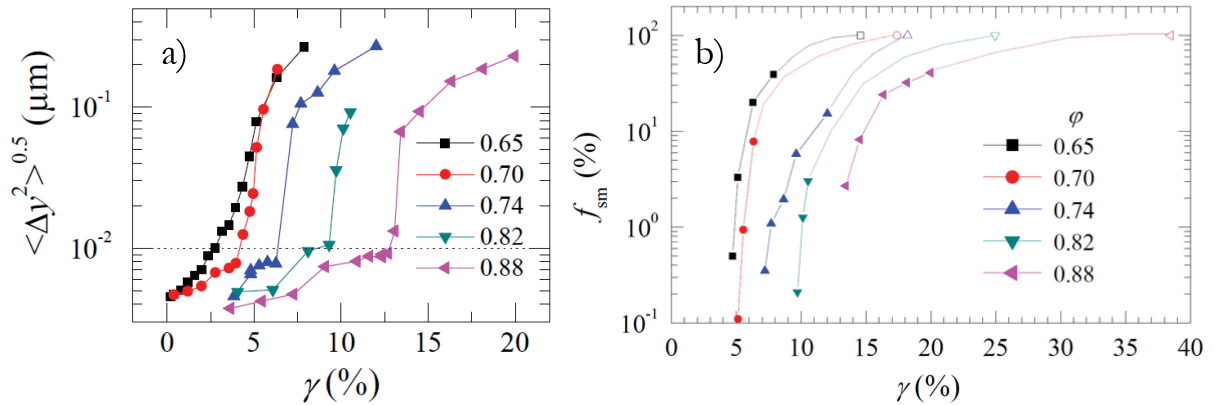


Figure 1.16: Concentrated emulsion. (a) Shear dependence of the rms displacement per shear cycle in the y direction (perpendicular to the applied shear). Data are labeled by the emulsion volume fraction. The dotted line is the threshold used to define the microscopic yield strain, γ_y . (b) Solid symbols: fraction f_{sm} of the "supermobile" drops. The abscissa of the open points correspond to the rheological crossover strain γ_c , where the sample is fluidized. The dotted lines are guides to the eye, consistent with the hypothesis that full fluidization may occur when all drops are supermobile, i.e. for $f_{sm} = 100\%$. Adapted from [Knowlton 2014].

microscopic dynamics under oscillatory shear is to monitor the evolution of the system across one full shear cycle, as it is done for example by Knowlton *et al.* on concentrated emulsions [Knowlton 2014]. The macroscopic rheology of the emulsions again resembles qualitatively Figs. 1.2 and 1.15, with a rather smooth and broad yielding transition that can be characterized by different "yield strains" (cf. Fig. 1.2). In order to shed light on the microscopic origin of yielding, the authors consider as relevant parameter the root mean square displacement $\langle \Delta y^2 \rangle^{0.5}$ of droplets observed stroboscopically, i.e. at two times separated by one full period, in the direction perpendicular to shear.

As expected, no significant irreversible motion is detected at the smallest strain amplitudes, where the emulsion deforms in an elastic, reversible way and all drops appear to be stroboscopically immobile within the measurement noise. With increasing deformation amplitude, however, $\langle \Delta y^2 \rangle^{0.5}$ exhibits a sharp increase (Fig. 1.16a) beyond a microscopic yield strain $\gamma_{y,micro}$, which proves to be much smaller than the crossover strain where $G' = G''$ (γ_f in Fig. 1.2), and closer to the yield strain (γ_y in Fig. 1.2) defined as the onset of the shear thinning regime. More in detail, the authors show that the sudden increase in $\langle \Delta y^2 \rangle^{0.5}$ is linked to the appearance of a population of mobile drops undergoing large deformations. Mobile drops initially represent a minority of the total drops, and they are spatially organized in mobile regions of the sample. Moreover, a careful analysis of the probability density function for irreversible displacements shows that the mobile drops can be further divided in two classes, with different mobilities. When the strain amplitude is increased beyond $\gamma_{y,micro}$, the drops belonging to the population with high-

est mobility, called "supermobile", grow in number while maintain their mobility fixed, until their fraction f_{sm} approaches 100% at a finite strain amplitude (Fig. 1.16b), close to the crossover between G' and G'' . This is consistent with the idea that full fluidization occurs when all (or at least the majority of) the particles are supermobile.

Besides demonstrating the power of real space analysis made possible by microscopy, the global picture presented by Knowlton *et al.* appears to be very instructive in light of the ongoing debate on the nature of the reversible to irreversible transition. In particular, the abrupt jump of the mean square displacement, associated with the appearance of a mobile population that counts an increasing fraction of the total drops, approaching unity at complete fluidization, is strongly suggestive of a first-order transition. In the work of Knowlton *et al.* a clear consistent picture could not be obtained, thus this remains a fascinating hypothesis, which stimulates future work in the field.

If Knowlton *et al.* only focus on stroboscopic experiments, much can be learned as well by following the full shear cycle, as it is done for example by Keim and Arratia on a crowded amorphous 2D assembly of colloidal particles segregated at the oil-water interface [Keim 2014]. An interfacial stress rheometer, based on a magnetic needle actuated by an electromagnetic field, is used to impose a controlled oscillatory stress to the suspension, and the macroscopic deformation, together with the local particle rearrangements, are probed by direct imaging of the interface. Although the general concept of the experiment is similar to the previous one, here the discussion is pushed beyond the stroboscopic analysis, and considers the detailed trajectory followed by each particle during the cyclic deformation. A purely stroboscopic analysis portrays a picture consistent with the one suggested by Knowlton *et al.*, with a first linear regime, where the mechanical response is elastic and reversible, with no microscopic rearrangements, and a well defined onset of microscopically irreversibility, marking a clear microscopic yielding transition beyond a critical amplitude γ_y . However, by analyzing the detailed particle trajectories, the authors argue that a more complex phenomenology hides behind this simple picture. Indeed, even in the linear elastic regime, particle motion is not perfectly affine, a phenomenon that can be interpreted as a consequence of the disordered structure. Even more interestingly, between the true linear regime and γ_y , an interesting intermediate regime is found, characterized by the presence of reversible plastic events. In this regime, the material is still stroboscopically static, but time-reversibility is broken by reversible plastic events that introduce hysteresis in the structural response. As a consequence, this dynamics, while being reversible upon one full cycle, dissipates energy, and contributes to the increase of the loss modulus, which indeed is found to deviate smoothly from its linear value slightly before γ_y . According to the authors, this observation might explain the apparent contrast between the sharp onset of microscopic irreversibility and the smoother transition observed in the viscoelastic properties.

An analogous result is obtained by Höhler *et al.* on aqueous foams, by using multiple light scattering in the DWS regime as a microscopic probe [Höhler 1997]. This technique allows one to probe extremely small rearrangements of the foam bubbles, which are

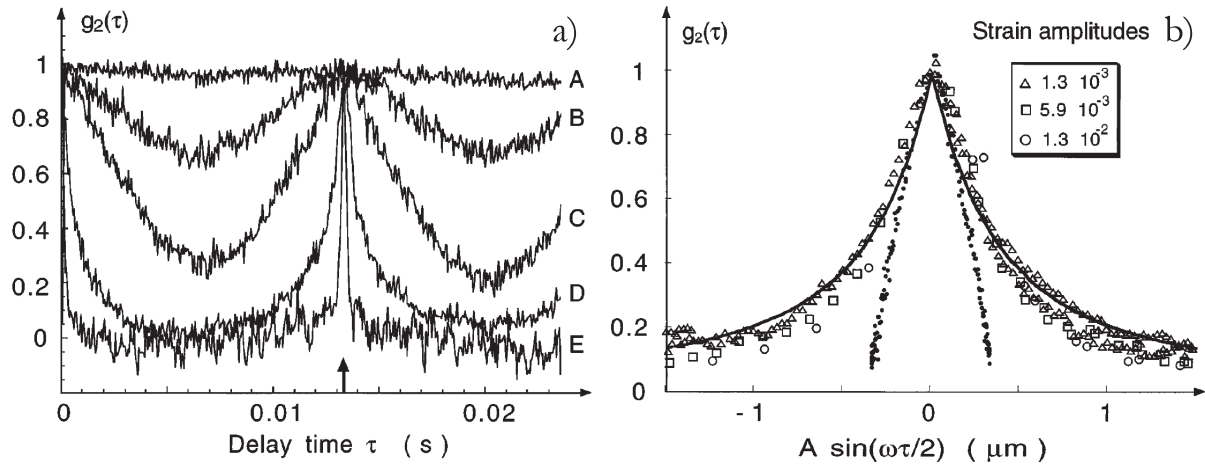


Figure 1.17: Aqueous foam. (a) Intensity autocorrelation data $g_2(\tau)$ plotted as a function of delay time τ . The curve labeled A has been obtained for a quiescent foam, whereas the other data sets have been measured at increasing strain amplitudes from B to E. The arrow indicates the period of the externally applied oscillating strain (correlation echo). (b) $g_2(\tau)$ represented as a function of the reduced variable $A \sin(\omega\tau/2)$ chosen to make plastic rearrangements apparent. The full line corresponds to the reversible plasticity model. To facilitate the comparison with the correlation produced by purely elastic deformation, one amplitude from the true linear regime has also been included, using small filled circles. Adapted from [Höhler 1997].

quantified in terms of an intensity correlation function $g_2(\tau)$, represented in Fig. 1.17a as a function of the time delay τ . The oscillatory deformation of the foam reflects in the observed oscillations of $g_2(\tau)$, which displays peaks for time delays equal to integer multiple of the oscillation period T , and it drops for intermediate τ values of an amount depending on the strain amplitude γ_0 . The peak at $\tau = T$ is the so-called correlation echo, and it contains information on microscopic reversibility: the peak value around 1 proves that at all strain amplitudes investigated the deformation is entirely reversible. On the other hand, detailed information on particle trajectories is encoded in the full shape of $g_2(\tau)$, which reveals that, within each shear cycle, reversible plastic rearrangements start occurring beyond $\gamma_y \sim 0.05\%$, remarkably below the yield point probed by rheology. The observation of reversible plasticity with DWS is much less straightforward than it would be in direct space analysis, and in order to make plastic rearrangements apparent, the authors replot their correlation data as a function of a rescaled variable (Fig. 1.17b). In this representation, $g_2(\tau)$ functions at different values of γ_0 are expected to collapse if the deformation is purely elastic. The fact that large amplitudes (open symbols in Fig. 1.17b) exhibit an upwards deviation from the trend observed in the linear regime (small filled symbols) is the sign that during each cycle the foam is periodically rearranged, such that each particle on average is displaced less than expected. This result, together with the previous ones, shows that the interplay between microscopic dynamics and nonlinear

rheological properties is complex, and it might exceed the intuitive notion of microscopic reversibility.

A slightly different insight into this interplay comes from a series of papers from Petekidis *et al.* [Petekidis 2002a, Petekidis 2002b, Petekidis 2003], who study the shear-induced microscopic rearrangements in colloidal glasses of hard spheres at different concentrations. The microscopic dynamics are probed again by DWS, giving access to intensity correlation functions qualitatively similar to the ones of Fig. 1.17. With respect to Höhler *et al.*, here the deformations are much larger, so that the authors have to restrict their analysis to time delays very close to the correlation echoes, since elsewhere $g_2(\tau) - 1 \approx 0$. Another relevant difference with respect to the previous work is that here the spontaneous Brownian motion of the particles contributes to a substantial decorrelation of higher order echoes even in the linear regime. Thus, in order to emphasize the role of shear-induced rearrangements, the authors normalize the echo peak height by its low strain amplitude limit. The result is shown in Fig. 1.18 as a function of γ_0 for samples at different volume fractions ϕ . The complexity of the figure is rationalized by identifying, for each strain amplitude, two characteristic strains: a smaller one, γ_{c1} (top arrows), indicating the first departure from unity, and a larger one, γ_{c2} , indicating complete disappearance of the echo. A parallel with the work of Knowlton *et al.* can be drawn by interpreting γ_{c1} as the onset of microscopic irreversibility, and γ_{c2} as the strain at which complete fluidization occurs. In particular, the authors discuss the unexpected large values of γ_{c1} , which can be as large as 15% at $\phi = 0.623$ and comes together with the surprisingly large recoverable elastic strains (again around $\sim 10 - 15\%$) that those materials can tolerate before yielding. The authors explain this behavior with the concept of cage elasticity, which they define as the ability of a particle and its cage of neighbors to undergo significant distortion while still retaining its identity. A comparison with rheology shows that for the concentrated samples deviations from linearity can be observed already at strains significantly smaller than γ_{c1} : thus, reversible plastic rearrangements must take place in colloidal glasses as well.

The result is even more apparent at the lowest concentrations (still beyond the glass transition), where γ_{c1} is small, implying that complete reversibility is lost rather early, but the correlation remains significant up to very large deformations, beyond 50%, a value several times larger than the yield strain of the material. This implies that several rearrangements have to occur in sequence within one oscillation: therefore the trajectory of particles must be tortuous, but it must also be largely reversible, which is rather unexpected. In an attempt to explain this phenomenon, the authors refer to an argument that would be more completely disclosed by Pine *et al.* in more recent years, with reference to microscopic reversibility in diluted suspensions [Pine 2005]. They argue that since the equations describing hydrodynamic flow at low Reynolds numbers are symmetric upon time reversal ($t \rightarrow -t$), particles' trajectories should always be reversible in absence of Brownian motion. Thus, they attribute the onset of irreversibility to Brownian motion, whose effectiveness at introducing irreversibility into the particle trajectories increases steeply on approaching random close packing, which explains the monotonic decrease of

γ_{c2} with increasing ϕ .

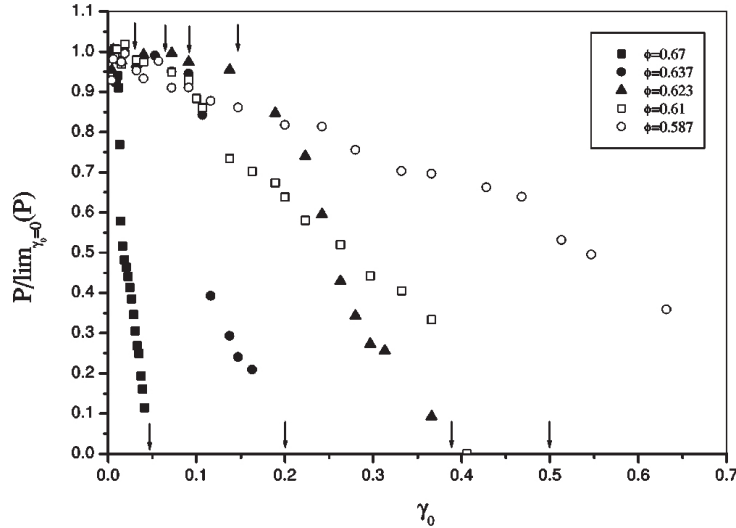


Figure 1.18: Hard sphere colloidal glass. Strain dependence of the relative first echo height ($P/\lim_{\gamma_0 \rightarrow 0} P$) at several volume fractions as indicated. Presenting the data in this form removes the effect of Brownian motion. Thus, when $P/\lim_{\gamma_0 \rightarrow 0} P = 1$ the sample strains elastically, and any reduction below 1 implies irreversible shear-induced rearrangements. Adapted from [Petekidis 2002a].

These examples show that, by comparing the system before and after a cyclic shear of amplitude γ_0 , a rich and complex phenomenology is found, which is further complicated by the observation of reversible plastic deformations, contributing to nonlinear rheology but not to stroboscopic dynamics. In an attempt to rationalize the results, we can identify several regimes: (1) a true linear regime at small γ_0 , where microscopic dynamics are thermally-activated, and eventual nonaffine deformations only stem from the heterogeneity of the structure; (2) a regime where nonlinear rheology might coexist with microscopic (full-cycle) reversibility, as a consequence of reversible plasticity; (3) the onset of microscopic irreversibility beyond a microscopic yield strain; (4) a gradual and generally complex transition where microscopic reversibility is progressively lost and the mechanical response evolves towards full fluidization; (5) a terminal regime, characterized by liquid-like, microscopically irreversible response.

This picture is intriguing, and calls for a deeper investigation of the microscopic processes observed under shear. One natural way to complete the above observations is to extend the analysis from one to several shear cycles, which can help elucidating the nature of irreversible rearrangements (e.g. diffusive, ballistic or something still different) observed in the various regimes. This will be discussed in the next paragraph.

1.3.3b Dynamic fatigue and damage accumulation

Oscillatory shear has the very appealing property of allowing one to investigate the sample in a stationary state: provided that such state exists and can be experimentally reached, it represents a convenient way to investigate the sample mechanical properties, since successive repetitions of the same measurement yield the same result, regardless the complex history of the material. However, when working with disordered, out-of-equilibrium materials, stationarity becomes a delicate concept because of the intrinsic aging dynamics characterizing most of them. As a consequence of aging, the viscoelastic moduli measured in the linear regime display a typically slow evolution in time, which may be safely neglected if the experimental time is short enough. However, one rarely discussed yet important aspect is that nonlinear rheology calls stationarity into play once again. Indeed, the slow time evolution of the mechanical properties measured in the linear regime can be accelerated by additional shear-induced processes, as it is captured for example by the above mentioned fluidity model [Derec 2003] or in a more complex way by theories like mode coupling theory [Yamada 1975, Reichman 2005] or soft glassy rheology [Sollich 1998]. Therefore, under nonlinear solicitations, stationarity may be more difficult to guarantee, so that care has to be taken in the interpretation of the experimental results. This remark might include as well the works mentioned above, since in the presence of strong shear-induced aging the yielding transition can look different when probed with different protocols [Perge 2014]. This effect is very well known since XIX century, when engineers discovered that a bridge designed to withstand the weight of several trains could collapse under the repeated transit of just one train. In a more controlled experiment, one would observe that oscillatory shear with amplitude slightly beyond the linear regime progressively weakens the material, until delayed failure may be observed. This weakening is sometimes called dynamic fatigue, as opposed to the static fatigue observed during creep. Despite the important similarities shared by the two phenomena, which have sometimes inspired intriguing, yet arguable direct analogies [Gibaud 2010], the two delayed failure mechanisms are distinct, and a comparison between the two may be very instructive. We will see an example in chapters 6 and 7. Moreover, the possibility of controlling and predicting delayed dynamic fatigue failure would have an enormous impact in real life applications, which further motivate to address this second mechanism in detail.

The delicate interplay between aging and yielding is discussed in detail using a soft colloidal glass as a model system by Rogers *et al.* [Rogers 2011], who investigate the complex memory of the sample by subjecting it to different oscillatory shear histories, both in a strain-controlled and in a stress-controlled fashion. As expected, the authors observe that aging is only slightly affected by small amplitude oscillations, whereas under large shear amplitudes the sample is fully rejuvenated during each cycle, so that stress and strain imposed protocols yield similar results in the two opposite regimes. However, as intermediate shear amplitudes are imposed, the behavior becomes more complex and dependent on whether the aging protocol was stress- or strain-imposed. A first conclusion

drawn by the authors from this observation is that under moderately nonlinear shear the material exhibits a faster evolution towards stiffer, more homogeneous configurations, since the imposed deformation helps the system to explore the free energy landscape, sooner locating deeper minima. Moreover, by further increasing the shear amplitude closer to the yield point, the authors argue that yielding is a gradual process: when the applied stress or strain in an amplitude sweep causes an event that would ultimately lead to yielding under those conditions, sufficient time must be allowed to elapse in order for that event to fully propagate and for yielding to occur.

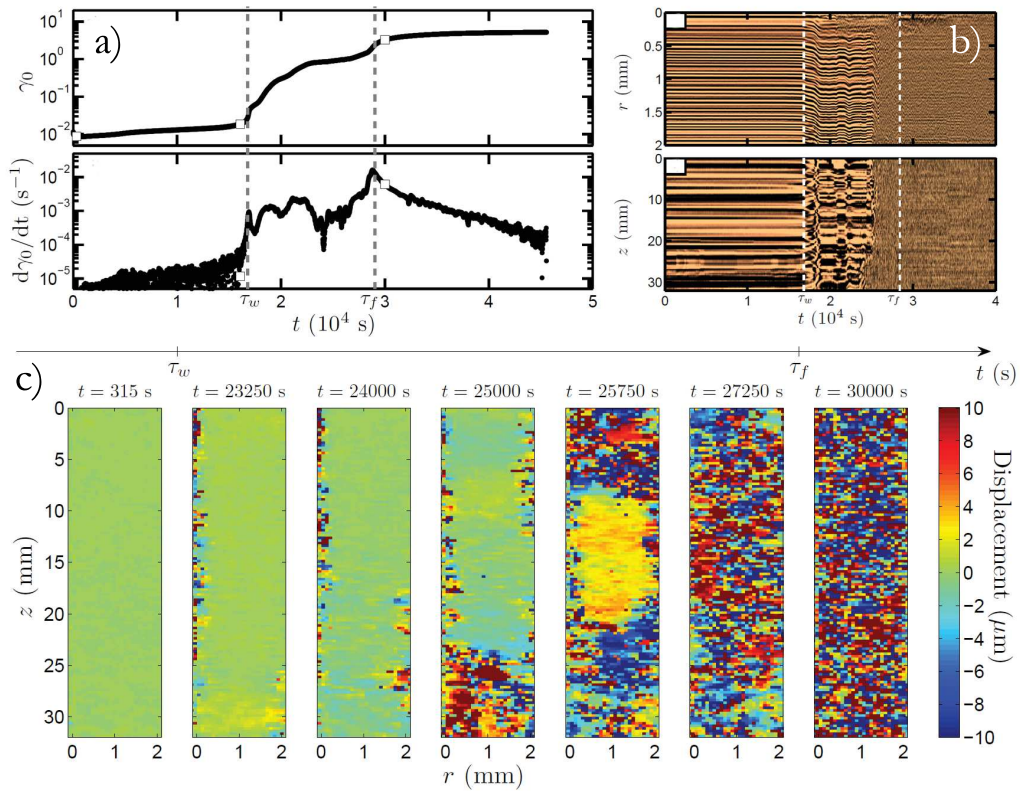


Figure 1.19: Carbon black gel. (a) Time-resolved LAOStress experiment illustrating the yielding and fluidization under an oscillatory stress of constant amplitude σ . Gray dashed lines indicate two characteristic times: the time τ_w such that $G'(\tau_w) = G''(\tau_w)$, which defines apparent yielding, and the time τ_f at which $d\gamma_0/dt$ reaches a global maximum, which corresponds to full fluidization as inferred from ultrasonic imaging. (b) Spatiotemporal diagrams of the ultrasonic speckle images recorded simultaneously to the rheological data shown in panel (a). White dashed lines indicate τ_w and τ_f . (c) Images of the displacement field $\Delta(r, z, t)$ between two successive ultrasonic pulses at various times during the yielding process. Adapted from [Perge 2014].

If this result is true for a colloidal glass like the one investigated by Rogers *et al.*, it is all the more true for network forming systems like colloidal or polymer gels, where a small damage in the stress bearing network reflects in a significant change in the mechanical

properties, which may also imply catastrophic delayed failure beyond a given level of damage. This effect is extensively addressed by Manneville and coworkers with stress imposed LAOS on different gels, namely carbon black gels [Gibaud 2010, Perge 2014] and protein gels [Saint-Michel 2017]. Their experiments consist in applying an oscillating stress with amplitude σ_0 below the yield stress and to follow the amplitude $\gamma_0(t)$ of the resulting deformation as a function of time spent under oscillatory stress. The authors observe that even for stress levels much below the yield stress, $\gamma_0(t)$ is not constant, but slowly increases over time, in a sublinear growth which is read as a manifestation of fatigue. This interpretation is confirmed by the direct observation of delayed fatigue failure, occurring after a waiting time τ_w (Fig. 1.19a). At τ_w , the amplitude $\gamma_0(t)$ displays a strong, sudden acceleration, and enters in an unstable regime characterized by strong temporal fluctuations of its time derivative $d\gamma_0/dt$. This unstable regime lasts until a second characteristic time τ_f , after which the strong fluctuations disappear and $\gamma_0(t)$ approaches a plateau value. While Saint-Michel *et al.* try to predict such delayed failure by looking at an intriguing, yet obscure, power-law scaling of higher order harmonics as a function of the instantaneous amplitude [Saint-Michel 2017], here we are rather interested in understanding the microscopic processes occurring in the sample during the three regimes identified by rheology, with particular focus on the change in dynamics detected close to the two characteristic times τ_w and τ_f . To this aim, Perge *et al.* complement their rheological measurements with a more local insight obtained by the already introduced ultrasound scattering technique. In particular, here the authors fully exploit the coherence of their scattering signal $S(z, r, t)$: following its stroboscopic evolution (Fig. 1.19b), they find that the speckles are mostly static until τ_w , which means that the scatterers are essentially stroboscopically immobile during the first induction time. This is reminiscent of a solid-like behavior, corroborated by the fact that here $G' > G''$. In the opposite regime, after τ_f , the opposite situation holds, and the scatterers are completely rearranged after each shear cycle: this is instead suggestive of a liquid-like behavior, consistent with the dominating loss modulus G'' . The intermediate situation is also intriguing, and it is better addressed in Fig. 1.19c, where a cross-correlation of the speckle images was used to extract the displacement maps. The authors argue that for waiting times between τ_w and τ_f , the results can be interpreted as the gradual fluidization of the gel, starting at time τ_w with slip at the inner moving wall and attaining completion at time τ_f .

The gradual fluidization process observed by Perge *et al.* consolidates the result obtained by Rogers *et al.*, and suggests that the gradual nature corresponds to a progressive erosion of solid-like domains starting from the boundaries (Fig. 1.19c).

The slow process of damage accumulation can also be usefully investigated by coupling the macroscopic deformation to a more direct probe of the microscopic dynamics. With respect to the previous experiments discussed, dynamic fatigue experiments are particularly challenging for direct space approaches based on particle tracking, which proved to be very effective in detecting displacements across one cycle, because of the important and potentially out-of-plane rearrangements. For this reason, scattering techniques prove to be more convenient, because they measure collective dynamics, with no need

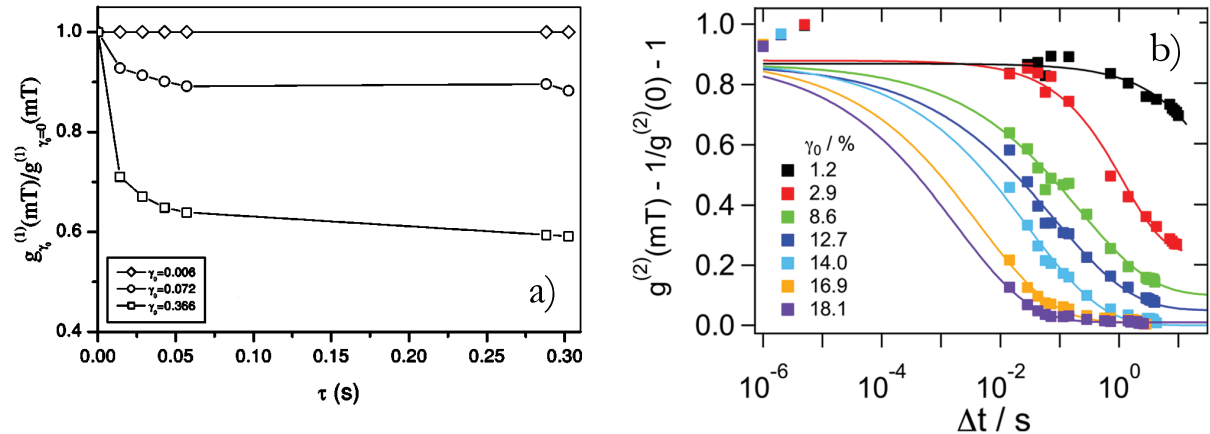


Figure 1.20: (a) Hard spheres colloidal glass. Decay of high order echoes at various strain amplitudes is represented by the ratio of the amplitude of the m th echo at a strain γ_0 to the corresponding amplitude at the lowest strain. This ratio takes into account the decay of the high order echoes due to Brownian motion (adapted from [Petekidis 2002a]). (b) Colloidal gel. Decay of high order echoes at various strain amplitudes, fitted by stretched-exponential functions Adapted from [Laurati 2014].

of identifying single particles. For example, Hébraud *et al.* [Hébraud 1997] study shear-induced rearrangements in concentrated emulsions with DWS, by following the decay of higher order correlation echoes. They find that, after the first correlation drop from $g_2(0) - 1 = 1$ to the value of the first correlation echo, a quasi-plateau is reached, with the level higher order echoes remaining essentially the same of the first one. The authors conclude that most of the rearrangements occur within one shear cycle, and they only discuss the decay of the first correlation echo. On the other hand, Petekidis *et al.* perform a similar experiment on colloidal glasses [Petekidis 2002a], and find that actually higher order correlation echoes slowly decay towards an apparent plateau value, which they call nonergodicity parameter (Fig. 1.20a). Again different is the result obtained by Laurati *et al.* [Laurati 2014] on colloidal gels, where full decorrelation is observed in the long time limit, which suggests that the apparent plateau value observed by Petekidis *et al.* might correspond to a slower relaxation mode. Interestingly, here the authors find that the decay of higher order correlation echoes is well described by a stretched exponential relaxation with a characteristic time rapidly decreasing with increasing strain amplitude beyond yielding (Fig. 1.20b).

Such an acceleration of microscopic dynamics observed at large amplitudes is very interesting if compared with the above mentioned models like the fluidity model, where a $\dot{\gamma}$ -dependent structural relaxation time was postulated: although to the best of our knowledge a comparison has never been attempted, perhaps the correlation echo experiments might represent an interesting way to check the microscopic implications of those models, which prove to describe rheology very accurately. In order to achieve such a quantitative comparison, however, one needs to obtain information about the nature of

the dynamics and their spatial heterogeneities. DWS can easily be performed in a space-resolved fashion [Nagazi 2016], but it is much more difficult to distinguish e.g. ballistic from diffusive motion with such technique. For this reason, single scattering techniques are also appealing, because such distinction can be done by comparing the relaxation times at different scattering vectors q (cf. chapter 2).

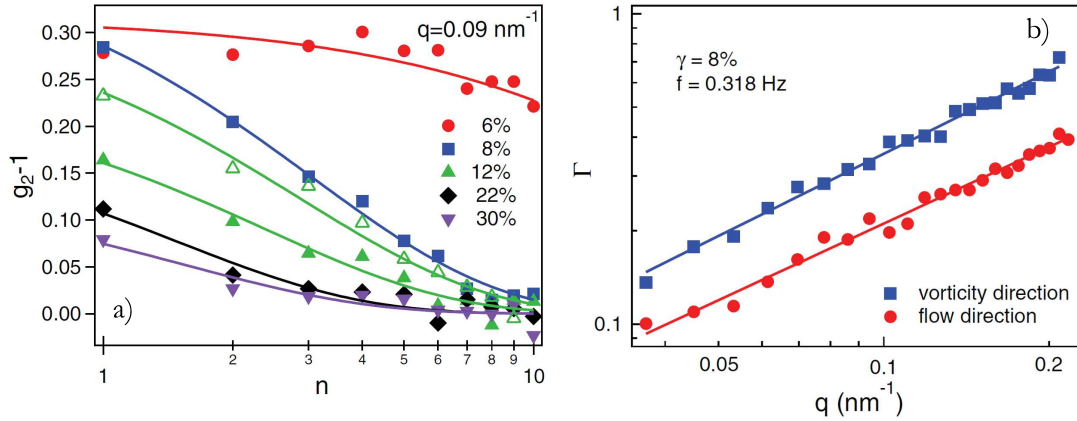


Figure 1.21: Colloidal gel. (a) Echo-peak amplitudes at one representative scattering vector $q = 0.09\text{nm}^{-1}$ along the vorticity direction as a function of delay cycle for different strain amplitudes. Also shown are echo peaks obtained at $\gamma = 12\%$ along the flow direction (open green triangles). Solid lines are exponential fits. (b) Echo-decay rate Γ (in 1/cycle) at one representative amplitude $\gamma = 8\%$ as a function of scattering vector q oriented in the flow direction (red circles) and in the vorticity direction (blue squares). Solid lines represent power-law fits. Extracted from [Rogers 2014].

One of the first examples is represented by the work of Rogers *et al.*, who probe the internal dynamics of a colloidal gel under cyclic shear using X-ray photon correlation spectroscopy (XPCS) [Rogers 2014]. The authors discuss different scattering vectors oriented both along the flow direction and perpendicular to it (in the vorticity direction). An overview of their results is represented in Fig. 1.21a. For the representative scattering vector shown, the decay of correlation echoes coincides with the spontaneous dynamics for strain amplitudes lower than 6%, whereas it becomes much faster starting from 8% deformation. This allows to locate the transition to irreversible deformation to a threshold $\gamma_c \sim 7\%$, higher than the strain at which the deviation from linear viscoelasticity is observed ($\gamma_{nl} \sim 2\%$), which suggests the presence of reversible plasticity. In the probed range of scattering vectors and strain amplitudes, the authors find that the decay of the correlation echoes is well fitted by single exponential decays, from which a relaxation rate $\Gamma(q, \gamma_0)$ can be extracted, shown in Fig. 1.21b. Interestingly, there is evidence that dynamics is non-isotropic, but it is faster in the vorticity direction, which is unexpected. Even more interestingly, $\Gamma(q, \gamma_0)$ exhibits a clear power-law dependence on the scattering vector, which is exploited by the authors to infer the spatial-size distribution of the single plastic events occurring under shear. By means of a simple scaling argument, the authors

conclude that the characteristic length scales rearranged by plastic events during LAOS at one given strain amplitude follow a power-law distribution, which is read as the sign that yielding can be described as a non-equilibrium critical transition. Without entering into the details of this discussion, we observe that an analysis of this kind has the potential to truly shed new light on the interdependence of microscopic dynamics and macroscopic nonlinear rheology, which is a key aspect determining the dynamic fatigue of materials.

1.3.4 Conclusion

To conclude, this (far from exhaustive) overview has shown that a huge effort has been put in recent years to characterize the failure mechanisms of soft materials. Although the phenomenology is generally very rich and complex, showing features that are often sample- and protocol-related, some knowledge has been acquired on the conditions under which a sample may flow viscoelastically or exhibit failure, either in a ductile-like manner or in a brittle-like manner. Failure process is most easily investigated in steady-rate experiments, where failure is expected to occur at large Weissenberg number $Wi = \dot{\gamma}\tau > 1$, where $\dot{\gamma}$ is the imposed shear rate and τ the longest relaxation time in the system. In those experiments, it was shown that deeper insight on the microscopic origin of failure can be obtained by coupling rheology with a microscopic characterization of the microscopic structure and dynamics, coming either from microscopy or from static scattering. These works have shown that brittle fracture occurs as a consequence of a cascade of break-up events weakening the stress-bearing backbone of the structure and triggering mechanical instability. However, the amount of bond breaking needed to produce such failure is still unclear, and likewise it is somehow controversial the nature and the amount of plastic events occurring during sample deformation before failure.

The investigation of delayed failure under a constant load is slightly more complex, not only because of the long and often unpredictable failure times, but also because of the complex time-dependence of the deformation rate during the induction time, which represents an additional challenge for techniques oriented at a microscopic characterization of the dynamics during creep. However, it turns out that the nature of those plastic dynamics and their temporal and spatial distribution might represent an important indicator, potentially opening the way towards a better control of delayed failure. To this end, a crucial aspect emerging from experiments is to be able to distinguish reversible from irreversible dynamics. At the macroscopic level, such distinction is addressed with creep recovery, which shows that, depending on the specific sample and experimental conditions, creep may be completely or partially reversible. Since failure is typically an irreversible phenomenon, the detection of a transition from reversible to irreversible deformation can represent a fundamental first step towards failure prediction. It turns out that such detection, although possible in principle, is in practice extremely delicate, since the yielding transition observed by rheology is typically very smooth and gradual. However, it has also been shown that such smooth rheological behavior might correspond,

at the microscale, to a nontrivial, intermittent behavior, and it has been proposed that indeed the precursors of failure might be identified by an investigation of the microscopic dynamics. Therefore, such observation during creep appears to be very promising, but it is also very challenging, and despite some attempts to the best of our knowledge this has not yet been clearly demonstrated.

On the other hand, similar investigations have been performed under oscillatory shear, where a comparison between the system before and after a cyclic shear with a given amplitude makes irreversible displacements apparent. As a result of these investigations, a rich phenomenology has been revealed. Deformations are elastic and reversible in the linear regime and completely irreversible in the large amplitude limit, but the transition between the two regimes is far from well understood. Interestingly, recent experiments have shown that the shear-induced acceleration of structural relaxation can be characterized following the evolution of the system after many shear oscillations. This is experimentally challenging, but also very promising, since addressing the amplitude-dependent relaxation time might provide a quantitative link between microscopic rearrangements and macroscopic mechanical properties, which is a rather old but still very debated topic.

1.4 Outline of the thesis

In our work we address some of the above challenges by means of a novel experimental setup coupling a stress controlled shear cell, which will be described in chapter 3, with a small angle static and dynamic light scattering apparatus. We cope with the challenges described above, related to performing dynamic light scattering experiments under transient shear, by means of an advanced data analysis technique, which is introduced in chapter 4. As a first model system we choose to investigate a colloidal gel, which exhibits a peculiar power-law rheology discussed in chapter 5. The well-controlled fractal structure and dynamics, as well as the simple phenomenological model accounting for its linear rheology, make this sample the ideal system to study how structure and dynamics are affected by shear. Creep and delayed failure are addressed in chapter 6. We show that affine and nonaffine dynamics can be effectively observed. Although the shear rate appears to be smooth and featureless, at the microscale we can clearly detect a sharp transition to irreversible microscopic dynamics, which we can consider a microscopic dynamic precursor of the failure that would only happen hours later. Moreover, a detailed analysis of the precursor shows an intriguing interplay with the microscopic architecture of the sample, which represents an additional step in the investigation of the microscopic origin of the rheological behavior. On the other hand, in chapter 7 we investigate the linear to nonlinear transition as it is observed in oscillatory shear, and we show that such transition, which is again smooth when probed by rheology, corresponds to a very sharp acceleration of the structural relaxation, which eventually leads to delayed failure under oscillatory stress with moderate amplitudes. In chapter 8 we check the generality of our previous findings by investigating another sample, with completely different microscopic

structure, namely a dense packing of soft microgel particles. Finally, a conclusive chapter closes the thesis with a general discussion on the results obtained and on the perspectives that our work opens to future investigations.

Experimental Methods

Contents

2.1	Light Scattering	49
2.1.1	Basic principle	50
2.1.2	Small angle light scattering	52
2.1.3	Static light scattering (SLS)	53
2.1.4	Dynamic light scattering (DLS)	56
2.2	Rheology	59
2.2.1	Shear deformation: stress and strain	59
2.2.2	Linear viscoelasticity	61
2.2.3	Nonlinear viscoelasticity	65

As anticipated in chapter 1, the ability to couple the macroscopic characterization of the mechanical properties with an insight on the microscopic structure and dynamics is fundamental to tackle the challenging and fascinating issue of material failure and failure precursors. In this chapter, we briefly review the light scattering (section 2.1) and rheology (section 2.2) methods, which will be used throughout this thesis.

2.1 Light Scattering

A scattering experiment can be understood by drawing an analogy of how vision works. When we observe an object, what our eye detects is the response of the object to light illuminating it, and which we interpret as a property of the object itself (color, shape, ...). The general idea underlying a light scattering experiment is similar: an incident light beam interacts with the sample, and as a result a part of it is scattered in a different direction and collected by an optical system, which plays the role of our eye. The main difference with respect to sight is that instead of focusing on the image of the object, therefore distinguishing light coming from different parts of it, a scattering experiment typically studies the intensity scattered by the entire sample in the far field, for example by placing the detector in the focal plane of a lens, thus losing space-resolved information. This is a good method to access average (statistical) properties of the sample, related to its internal microscopic structure.

Different types of radiation other than visible light (for example X rays or neutrons) can also be employed in a scattering experiment, providing valuable complementary information to light scattering thanks to the specific interactions with the sample and the different length scales probed. However, once those differences are taken into account, all scattering experiments can be described to a large extent in a unified way: for this reason, the present section will only focus on light scattering.

2.1.1 Basic principle

A schematic of the basic scattering geometry is shown in figure 2.1. Coherent light from a laser is directed towards the sample, and the intensity scattered at a well defined *scattering angle* θ is collected by a photosensitive element, e.g. a photodiode. In what will follow, we will take the so-called first Born approximation, in which only a small fraction of the incoming beam is scattered: this corresponds to the single scattering regime, where light is scattered no more than once before reaching the detector.

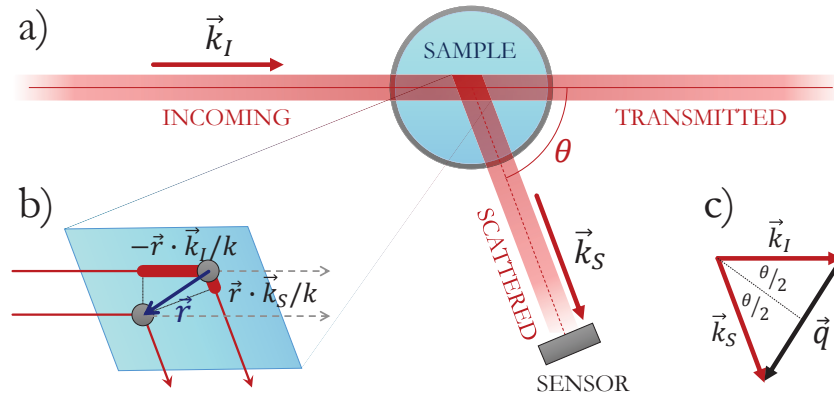


Figure 2.1: (a) General scheme of a light scattering experiment (top view): laser radiation (characterized by an incoming wavevector \vec{k}_I) illuminates the sample, and light scattered at a given scattering angle θ (with wavevector \vec{k}_S) is detected in the far field. In the first Born approximation, the transmitted beam is always much more intense than the scattered beam. (b) Closer look at the scattering volume, highlighting the contribution of two scatterers, at relative distance \vec{r} . The difference in optical path between the two scattered waves is represented by the thick lines, whose total length Δs is given by Eq. 2.2. (c) Geometric construction of the scattering vector \vec{q} , whose modulus is calculated using Eq. 2.3

In order to understand the intensity pattern of scattered light and extract from it some information on the sample, a theoretical model is needed. Two complementary approaches are possible:

- A *continuous*, statistical approach: one can define a response function $\varepsilon(\vec{q}, \omega)$ (well defined in the Fourier space, thus nonlocal), which relates the external perturba-

tion to the system response, i.e. the variation of an observable quantity coupled to the perturbing field. For light scattering, the probe is the electric field, and the response function is the polarizability, a quantity simply related to the refractive index $n(\vec{x}, t)$. The scattered light can thus be linked to the presence of local fluctuations in $n(\vec{x}, t)$, from which one can learn important details about the structure of the sample. Moreover, the time dependence of $n(\vec{x}, t)$, revealed by temporal fluctuations in the scattered light, can be analyzed to get an insight on the sample dynamics.

- A *discrete* approach, starting from one point-like constituent. Its interaction with the incoming beam results in a scattered spherical wave, with a characteristic intensity distribution. Waves scattered by each particle inside the sample superpose in the far field, creating a complex interference pattern (a *speckle* pattern), encoding detailed information about particle shape, size, position and dynamics. This section will follow this second approach, showing how to extract valuable information from the static properties of the speckle pattern and from its temporal fluctuations.

From classical electrodynamics [Jackson 2007], it is known that, when a single charge is accelerated by an electromagnetic wave, it emits a spherical wave, whose intensity profile follows the so-called dipole distribution:

$$\frac{dP_{ed}}{d\Omega} = \frac{ck^2}{8\pi} p^2 \sin^2 \varphi \quad (2.1)$$

where c is light's speed, $k = 2\pi n/\lambda$ is the wavevector of the incoming beam, with λ its wavelength in vacuum and n the refractive index of the medium, p is the induced dipole and φ is the angle between the scattered beam and the polarization axis of the incoming beam, assumed to be linearly polarized. A speckle pattern can be understood as the interference of all spherical waves scattered by the sample: their number is huge, but the basic underlying principle can be grasped by considering the contribution of just two scattering elements (Fig. 2.1b). What makes the interference nontrivial is the relative phase factor coming from the different distance Δs traveled by the waves, which can be expressed as a function of the relative position \vec{r} of the two scatterers:

$$\Delta\phi = k\Delta s = (\vec{k}_S - \vec{k}_I) \cdot \vec{r} = \vec{q} \cdot \vec{r} \quad (2.2)$$

Here \vec{k}_S and \vec{k}_I are the scattered and the incident wavevectors respectively, which have the same modulus $k = \frac{2\pi n}{\lambda}$ since dipoles scatter light with the same wavelength as the incident light. Their difference $\vec{q} = \vec{k}_S - \vec{k}_I$ is called the scattering vector, which is the relevant parameter defining the lengthscale being probed by a scattering experiment. Indeed, one can easily see that the interference changes from constructive ($\Delta\phi = 0$) to destructive ($\Delta\phi = \pi$) for particle relative displacements $\delta r = \pi/q$ along the \vec{q} direction.

The scattering vector is related to the scattering angle θ by the simple relation (Fig. 2.1c):

$$q = 2k \sin \frac{\theta}{2} \quad (2.3)$$

Thus, the larger the scattering angle, the smaller the lengthscale probed, with a lower bound set by $\pi/q_{max} = \lambda/4n$ in the backscattering direction.

2.1.2 Small angle light scattering

Equation 2.3 shows that light scattering typically probes matter on lengthscales comparable to the visible wavelength, but that larger lengthscales (up to more than 100λ) can be probed by analyzing light scattered at small scattering angles, which can be very interesting in some cases, like the ones we will show in the next chapters.

A great advantage of small angle light scattering is that, as it is represented in Fig. 2.2, a multichannel detector (e.g. a CMOS camera) can be used to acquire the intensity scattered at several scattering vectors at the same time. Such detectors are typically much slower than photodiodes, and they also have a smaller dynamic range, but smart acquisition schemes like the one we have developed (see appendix A) and multiple exposure times can be used to improve the detection performance.

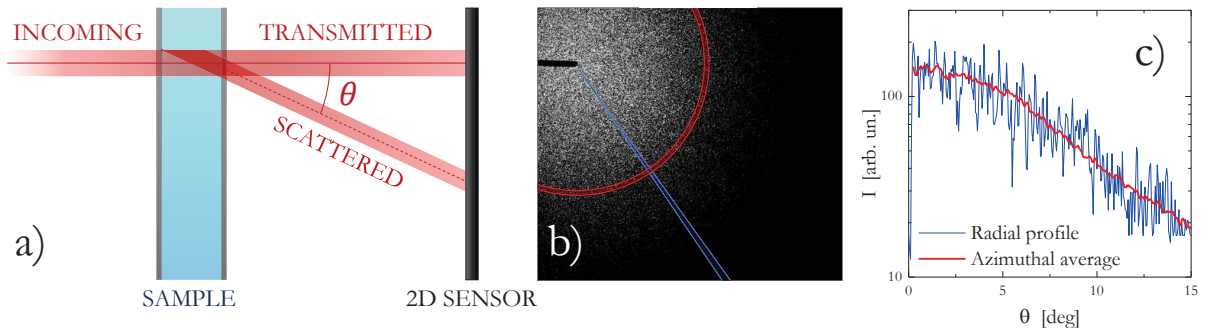


Figure 2.2: (a) General scheme of a small angle light scattering experiment: a flat scattering cell is chosen to improve the quality of the optical interfaces, and a multichannel sensor is used to detect several scattering vectors at the same time. In general, an optical system (not shown) is employed in order to collect the scattered light and send it to the sensor. More details can be found in [Tamborini 2012]. (b) Example of the speckle pattern detected in the far field. The transmitted beam is hidden by the beam stop in the top left corner, the scattering angle θ increases radially. (c) Radial intensity distribution (blue) observed along the blue sector highlighted in panel b, plotted together with the azimuthal average (red), obtained by averaging each scattering angle θ on the azimuthal angle (red circle in panel b).

The detection of light scattered at small angles poses a few technical challenges that have to be addressed with a specific experimental geometry, which may change significantly according to the desired range of scattering angles, the required sensitivity or other

technical constraints. The main challenge associated to small angle scattering comes from imperfections in the optic elements, which typically produce a spurious scattering signal greatly increasing at the smallest angles. The presence of the intense transmitted beam in the field of view of the detector also requires special care in the design of the setup. As a last challenge associated with small angle light scattering, aberrations in the optical system that collects the scattered light usually set a strong upper limitation in the accessible scattering angles.

In our work, we face these challenges with a custom made setup [Tamborini 2012], which uses a flat scattering cell and a complex optical system allowing one to remove the transmitted beam and reducing the effect of aberrations. The range of scattering angles that are typically accessed using this instrument lays in the intermediate range ($0.5^\circ < \theta < 25^\circ$) between the angles typically probed in wide angle ($\theta \gtrsim 20^\circ$) and small angle ($\theta \lesssim 5^\circ$) light scattering.

Figure 2.2b shows an example of speckle image acquired with our setup. Each pixel is associated to a scattering vector. The position of the $q = 0$ transmitted beam is on the top left corner, where the shadow of a beam stop is clearly visible. Superimposed to a radial smooth intensity decay, a speckle pattern of characteristic size slightly higher than one pixel is clearly visible. Different configurations of the same system would have the same overall q dependence of the scattered intensity, but the speckle pattern would be totally different, as a consequence of scatterers' microscopic rearrangement. This suggests that two distinct pieces of information can be extracted: the first deals with the slow smooth intensity decay, which is related to the internal structure of the sample, whereas analyzing the speckle pattern time fluctuations can provide information related to the scatterers' dynamics. These two different kinds of information are provided by static and dynamic light scattering, respectively.

2.1.3 Static light scattering (SLS)

2.1.3a Form factor and structure factor

Static light scattering provides averaged information on the internal structure of the sample, in terms of correlations between the scatterers' positions. For this purpose, the speckle pattern of Fig. 2.2b must be smoothed, by time or ensemble averages, for example by averaging over rings of pixels corresponding to nearly the same scattering angle θ in the case of isotropic samples. Starting from such an averaged profile (red line in Fig. 2.2c), we briefly sketch how static light scattering works by extending the previous discussion, from the interference between the electric field scattered by two scattering elements to a sum over all elements belonging to each of the N particles in the scattering volume. Each particle is indexed by $j = 1, \dots, N$, and contains a number M_j of scattering elements. The total scattered field is:

$$\vec{E}(\vec{q}) = \sum_{j=1}^N \sum_{l=1}^{M_j} \vec{E}_{jl}(\vec{q}) e^{i\vec{q} \cdot (\vec{r}_j + \vec{r}_l^{(j)})} = \sum_{j=1}^N \vec{E}_j(\vec{q}) e^{i\vec{q} \cdot \vec{r}_j} \quad (2.4)$$

where $\vec{E}_{jl}(\vec{q})$ is the electric field scattered by a single element (indexed by l) belonging to particle j . The position of the element in the sample is $\vec{r}_j + \vec{r}_l^{(j)}$, \vec{r}_j being the j -th particle center of mass position, whereas $\vec{r}_l^{(j)}$ denotes the position of the charge in the particle reference frame. In the second equality the sum over all the M_j scattering elements composing the j -th particle was factorized and called $\vec{E}_j(\vec{q}) = \sum_{l=1}^{M_j} \vec{E}_{jl}(\vec{q}) e^{i\vec{q} \cdot \vec{r}_l^{(j)}}$. This represents the electric field scattered by particle j (to within the phase factor $e^{i\vec{q} \cdot \vec{r}_j}$).

If all particles are identical and are illuminated by a uniform field, the scattered field $\vec{E}_j(\vec{q}) = \vec{E}_P(\vec{q})$ is the same for all particles and can be taken outside the sum. The scattered intensity can then be calculated as:

$$I(\vec{q}) = \vec{E}(\vec{q}) \cdot \vec{E}^*(\vec{q}) = \left| \vec{E}_P(\vec{q}) \right|^2 \sum_{j,l=1}^N e^{i\vec{q} \cdot (\vec{r}_j - \vec{r}_l)} = AP(\vec{q})S(\vec{q}) \quad (2.5)$$

where $P(\vec{q}) = |\vec{E}_P(\vec{q})|^2 / |\vec{E}_P(0)|^2$ is the so-called particle *form factor*, accounting for the single particle shape and size, $S(\vec{q}) = N^{-1} \sum_{j,l=1}^N e^{i\vec{q} \cdot (\vec{r}_j - \vec{r}_l)}$ is the sample *structure factor*, only dependent on the relative positions between the particles, and A is a proportionality constant, which will depend on instrumental parameters such as the laser beam size and intensity, as well on physical parameters such as the particle size, number density and refractive index contrast.

2.1.3b $P(q)$ and $S(q)$ for colloidal gels

The power of the factorization of the scattered intensity in the product of a form factor times a structure factor can be sketched in the case of the colloidal gels that will be presented in part II. Figure 2.3 shows three scattering curves, obtained by matching the results of several scattering techniques (small and wide angle light scattering, as well as small angle X ray and neutron scattering), for three different samples: (1) a diluted (particle volume fraction $\phi = 0.037\%$) suspension of colloidal particles, (2) a more concentrated ($\phi = 5\%$) suspension of the same particles interacting via a repulsive electrostatic potential, (3) a $\phi = 5\%$ suspension of the same particles with short range attractive interaction.

1. In the dilute suspension, the average interparticle distance is large and there is no correlation between the particle positions: as a consequence, the structure factor reduces to $S_{dil}(\vec{q}) = \langle e^{i\vec{q} \cdot \vec{r}} \rangle = 1$, and the measured scattered intensity is simply proportional to the particle form factor. The form factor of a sphere can be calculated by casting the sum over individual scattering elements into an integral over the particle volume V_j :

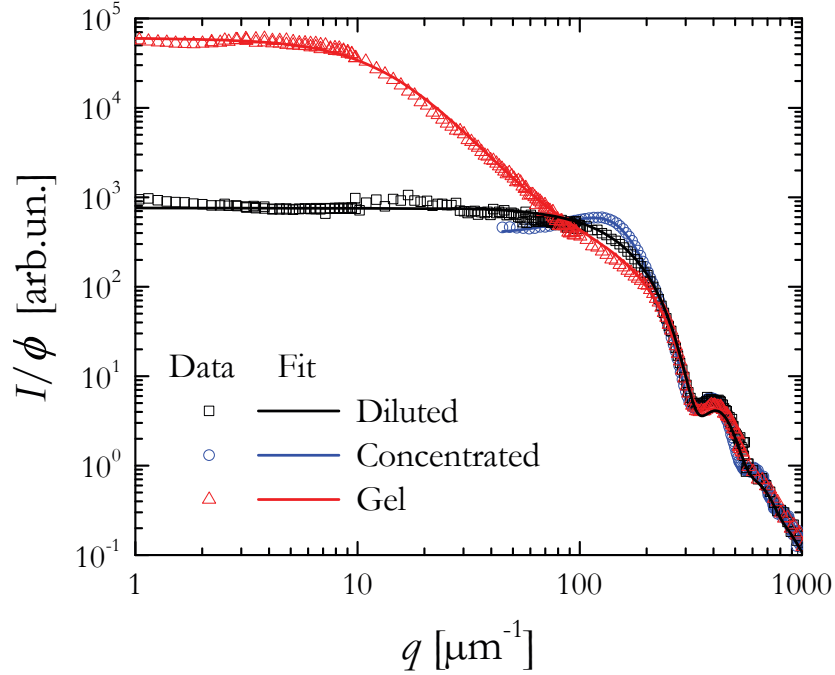


Figure 2.3: Static scattering signal plotted for three different colloidal systems, containing the same colloidal particles 1) diluted suspension ($\phi = 0.037\%$, black), from which the form factor can be extracted, carrying information about the average radius $\bar{R} = 12.5$ nm and size polydispersity $\sigma_R = 10\%$, 2) slightly concentrated suspension ($\phi = 5\%$, blue), with a structure factor peak at $qR \sim 2$ and a suppressed $I(q)$ at small scattering vectors, 3) an attractive colloidal gel ($\phi = 5\%$, red), displaying a fractal structure with fractal dimension $d_f = 2$ up to a characteristic lengthscale of about $0.5\mu\text{m}$.

$$P(\vec{q}) \propto \int_{V_j} \Delta\rho(\vec{r}) e^{i\vec{q}\cdot\vec{r}} d^3r \quad (2.6)$$

where $\Delta\rho$ is the contrast function, essentially proportional to the local density of scatterers. By assuming a uniform density inside a spherical volume, one obtains the form factor of a homogeneous spherical particle of radius R :

$$P_R(\vec{q}) = \left\{ \frac{3}{(qR)^3} [\sin(qR) - qR \cos(qR)] \right\}^2 \quad (2.7)$$

In Fig. 2.3, the form factor $P_R(\vec{q})$ was convoluted with a Gaussian size distribution peaked around an average particle size \bar{R} , to take into account sample polydispersity. A fit to the experimental data yields $\bar{R} = 12.5$ nm with a polydispersity $\sigma_R = 10\%$.

- As the number density of the particles is increased, the particle positions start to become correlated as a consequence of the interparticle interactions, and the structure function starts to play a nontrivial role in the observed intensity profile. A direct link between the pair correlation function $g(\vec{r})$ (i.e. the probability of finding a pair of particles whose relative position is \vec{r}) and the structure factor $S(\vec{q})$

comes from a decomposition of the double sum defining $S(\vec{q})$ in a "self" ($j = l$) term, which is exactly 1, and a "cross" ($j \neq l$) term, which can be cast into an integral corresponding to the Fourier transform of $g(\vec{r})$:

$$S(\vec{q}) = 1 + \int g(\vec{r}) e^{i\vec{q}\cdot\vec{r}} d^3r \quad (2.8)$$

For example, in a diluted suspension, a virial expansion of the equation of state provides an expression for the pair correlation function: $g(\vec{r}) = \exp[-v(\vec{r})/k_B T]$, where $v(\vec{r})$ is the interaction potential [Landau 2013]. A similar starting point leads with more sophisticated calculations to the Percus Yevick structure factor, which is used in Fig. 2.3 to fit the experimental intensity, using the factorization of equation 2.5 and the form factor obtained from the diluted sample [Vrij 1979]. Note that for the $\phi = 5\%$ suspension, the measured intensity clearly exceeds the value for the form factor at $qR \approx 2$: this is the sign of an emerging peak in $S(q)$, reflecting the fact that as particles get closer to each other the density fluctuates strongly on the length scale of the particle diameter, whereas a suppression of $S(q)$ for small q values reflects the fact that at large lengthscales the density is still rather uniform.

3. Finally, as the interparticle potential is turned into attractive, particles aggregate and form a complex structure spanning a large range of lengthscales. As a result, the structure function develops several interesting features, like a power-law regime, which is a consequence of the fractal structure of the particle clusters, terminating with a shoulder corresponding to the typical cluster size (see part II for more details about the sample structure). Here $P(q)S(q)$ was fitted by an analytic model assuming a distribution of fractal aggregates with fractal dimension $d_f = 2$ and an exponential size distribution with a typical size around 100 nm [Sorensen 1999].

2.1.4 Dynamic light scattering (DLS)

2.1.4a Conventional dynamic light scattering

While static light scattering deals with the smooth variation of the intensity with q , neglecting the detailed appearance of the instantaneous speckle field, dynamic light scattering focuses precisely on the latter, relating intensity fluctuations to the sample dynamics. Indeed, as already pointed out with Eq. 2.2, the bright (dark) spots that one calls speckles are regions of constructive (destructive) interference of light emitted by all scatterers, where the constructive or destructive nature changes if particles are displaced over a distance of the order of q^{-1} .

Thus, the basic principle of dynamic light scattering is to record the intensity fluctuations measured at one specific q vector, and to measure the characteristic time τ needed for a bright speckle to become dark or vice versa. In the schematic representation of Eq. 2.2, where only two scatterers contribute to the observed signal, this implies that the relative phase between the two interfering waves has changed of the or-

der of unity over that characteristic time, which in turn reveals a particle displacement $\langle \Delta \vec{r}(\tau) \rangle_t = \langle \vec{r}(t + \tau) - \vec{r}(t) \rangle_t \sim \lambda / \sin(\theta/2) \hat{u}_q$. Here \hat{u}_q is a unit vector pointing in the \vec{q} direction, which emphasizes that the relative displacement that one observes in dynamic light scattering is projected along the scattering vector. This observation is very relevant in the case of anisotropic dynamics, like the one induced by shear flow, and it will be developed in chapter 4.

An analogous result holds for the more realistic picture of N particles contributing to the scattered intensity. In this case, time dependence can be easily incorporated into Eq. 2.5, by assuming a time-independent form factor and a time-dependent structure factor:

$$I(\vec{q}, t) = AP(\vec{q})S(\vec{q}, t) \propto \sum_{j,l=1}^N e^{i\vec{q} \cdot [\vec{r}_j(t) - \vec{r}_l(t)]} \quad (2.9)$$

Thus, fluctuations of $I(\vec{q}, t)$ provide information on the *average* particle displacements along the scattering vector. Again, a decomposition of the double sum allows to distinguish between "self" dynamics and "collective" dynamics (typically dominant when $S(\vec{q}) \gg 1$), which are linked to collective relaxation of particle density fluctuations [Pusey 1978]. A quantitative measurement of the temporal fluctuations of $I(\vec{q}, t)$ can be obtained by computing the time autocorrelation function of the scattered intensity:

$$g_2(\vec{q}, t, \tau) = \frac{\langle I(\vec{q}, t + \tau) I(\vec{q}, t) \rangle}{\langle I(\vec{q}, t + \tau) \rangle \langle I(\vec{q}, t) \rangle} \quad (2.10)$$

where $\langle \dots \rangle$ denotes an ensemble average, which for ergodic samples can be measured experimentally by performing a time average lasting much longer than the characteristic relaxation time τ_R of g_2 (typically an average over $10^3 - 10^4 \tau_R$ is needed). The intensity autocorrelation function can be related to quantities that can be modeled theoretically, like the intermediate scattering function $f(\vec{q}, \tau)$, which essentially coincides with the ensemble averaged field correlation function:

$$f(\vec{q}, \tau) = \langle g_1(\vec{q}, t, \tau) \rangle_t = \frac{\langle \vec{E}(\vec{q}, t + \tau) \cdot \vec{E}^*(\vec{q}, t) \rangle_t}{\left| \langle \vec{E}(\vec{q}, t) \rangle_t \right|^2} \propto \left\langle \sum_{j,l=1}^N e^{i\vec{q} \cdot [\vec{r}_j(t+\tau) - \vec{r}_l(t)]} \right\rangle_t \quad (2.11)$$

The Siegert relation, which holds as long as the scattered field has Gaussian statistics, relates the intensity and field correlation functions [Berne 2013]:

$$g_2(\vec{q}, t, \tau) = 1 + |g_1(\vec{q}, t, \tau)|^2 \quad (2.12)$$

The intermediate scattering function, in turn, can be directly related to the internal dynamics of the sample: indeed, it represents the (spatial) Fourier transform of the van Hove distribution function $G(\vec{r}, t)$, which is the dynamic counterpart of the pair correlation function $g(\vec{r})$ [Hopkins 2010]:

$$\begin{aligned}
G(\vec{r}, \tau) &= \left\langle \frac{1}{N} \int \rho(\vec{r}' + \vec{r}, t + \tau) \rho(\vec{r}', t) d^3 r' \right\rangle_t \\
&= \left\langle \frac{1}{N} \int \sum_{j,l=1}^N \delta[r' + \vec{r} - \vec{r}_j(t + \tau)] \delta[r' - \vec{r}_l(t)] d^3 r' \right\rangle_t
\end{aligned} \tag{2.13}$$

where $\rho(\vec{r}, t) = \sum_{j=1}^N \delta[\vec{r} - \vec{r}_j(t)]$ is the density of a system comprising N particles and $\delta(\vec{r})$ represents Dirac's delta function. $G(\vec{r}, \tau)$ is the probability of finding at time τ a particle at position \vec{r} , given that a particle (not necessarily the same) was in the origin ($\vec{r} = 0$) at time 0. A substitution of Eq. 2.13 into Eq. 2.11 directly yields

$$f(\vec{q}, \tau) = \int G(\vec{r}, \tau) e^{i\vec{q}\cdot\vec{r}} d^3 r \tag{2.14}$$

Thus, the intermediate scattering function can be considered as the dynamic counterpart of the structure factor (Eq. 2.8).

As an example, we consider Brownian diffusion. In this case, the van Hove function is a Gaussian with variance $\langle \Delta r^2(\tau) \rangle = 6D\tau$, D being the diffusion coefficient. By Fourier transforming such distribution one obtains $f(\vec{q}, \tau) = \exp(-Dq^2\tau)$. One thus predicts an exponential decay of the field correlation, with a characteristic time $\tau_R = 1/Dq^2$. Thus, from the intensity correlation function measured on a Brownian suspension one extracts the diffusion coefficient D . In turn, D can be used to determine the hydrodynamic radius R_h of the particles if the solvent viscosity is known, using the Stokes-Einstein relation $D = k_B T / (6\pi\eta R_h)$, as it is routinely done in DLS-based particle sizing [Berne 2013]. Conversely, one can use known particles as probes, and extract from the DLS signal physical information about the solvent, like the viscosity: this is the essence of DLS-based microrheology.

2.1.4b Multispeckle and time-resolved correlations

Operationally, conventional DLS is based on the assumption that the ensemble average in Eq. 2.10 can be replaced by a time average. Ensemble and time averages are equivalent if, over the averaged time interval, the sample has been able to explore a statistically relevant subset of the phase space, i.e. for the so-called *ergodic* systems. Ordinary diluted suspensions usually fall in this class of systems, since their relaxation time is usually much smaller than 1 s, so that many independent configurations can easily be sampled within the duration of an experiment. However, there are several instances where the relaxation time exceeds 1 s by many orders of magnitude, as is the case for very viscous suspensions studied at small angles or even more importantly for out of equilibrium systems, like colloidal gels or glasses: these systems are said to be *nonergodic*, and require special care for the ensemble average in a DLS experiment to be properly evaluated.

One method is to sample $g_I(\vec{q}, t, \tau)$ for several independent speckles. This can be done by translating or rotating the sample during the measurement, or more conveniently

by detecting the fluctuations of several speckles at the same time using a multichannel detector, like a CMOS camera, and by averaging the contribution of all speckles. The resulting correlation function is:

$$g_2(\vec{q}, t, \tau) = \frac{\langle I_p(t + \tau) I_p(t) \rangle_{p \in ROI(\vec{q})}}{\langle I_p(t + \tau) \rangle_{p \in ROI(\vec{q})} \langle I_p(t) \rangle_{p \in ROI(\vec{q})}} \quad (2.15)$$

where $I_p(t)$ is the intensity detected by pixel p at time t , and $\langle \dots \rangle_{p \in ROI(\vec{q})}$ corresponds to an average over all pixels belonging to a region of interest (ROI) associated to a small region in q space centered around \vec{q} .

Such a technique, called multispeckle, allows one to achieve a good sampling of the gray levels of the speckle pattern, which corresponds to a good sampling of the microscopic configurations of the sample, provided that the scattering volume is larger than any structural and dynamical correlation length. Of course, the speckles averaged with this technique should provide equivalent information, thus they should correspond to nearly the same scattering vector, which sometimes sets a strong limitation, for example in the case of large speckles or of a strong q dependence of the dynamics, as it is the case under shear, as discussed in chapter 4.

More generally, this method provides properly averaged results without time averages, and thus allows one to characterize time-dependent dynamics, like ageing or transient processes. For this reason, such a method, called Time Resolved Correlation (TRC) [Duri 2005], is particularly adapted for probing a sample under shear.

2.2 Rheology

Rheology, as the Greek origin of the name suggests, is the study of the flow of matter. One commonly thinks of gases and liquids as mobile substances subject to flow and of solids as rigid materials that do not flow, but before the critical eyes of the rheologist, nature shows a much more rich and complex variety of behaviors, which one classifies as *viscoelastic*. Indeed, rephrasing the well known statement of Heraclitus from which the name "rheology" was coined ($\tau\alpha \Pi\acute{\alpha}\nu\tau\alpha \rho\acute{\epsilon}\iota$), everything flows, depending on the timescale and the external conditions [Traxler 1939].

2.2.1 Shear deformation: stress and strain

The above distinction between liquids, solids and viscoelastic materials concerns the mechanical properties of an object, i.e. the relationship between any force applied to it and the subsequent change in its shape and size. Both quantities can be generally quantified by tensorial variables: the stress $\underline{\underline{\sigma}}$, representing the force per unit surface acting on different faces of a small cubic element from different directions, and the deformation $\underline{\underline{\gamma}}$ (or its time derivative $\underline{\underline{\dot{\gamma}}}$), describing the relative changes in dimensions and angles of

that cubic element. In a generic deformation geometry, both stress and strain depend on the position \vec{x} , so that the relation between $\underline{\underline{\sigma}}$ and $\underline{\underline{\dot{\gamma}}}$ (the so-called rheological constitutive equation) is a very complex tensorial equation. However, there are a few specific types of uniform (homogeneous) deformations where stress and strain are independent of \vec{x} and assume a relatively simple form. One of them is simple shear, where two opposite faces of the cubic element are displaced by sliding. In this geometry (Fig. 2.4a), one can measure the shear couple $M = eF$, e being the gap separating the two surfaces and F being the force applied to them, and the relative linear displacement δ of the two surfaces. In terms of these quantities, the above tensorial relations reduce to scalar ones, connecting the (scalar) stress $\sigma(t) = F(t)/S$, S being the area of the two opposite faces, to the strain $\gamma(t) = \delta(t)/e$. In this thesis, with the only exception of appendix B, we will only focus on the shear geometry.

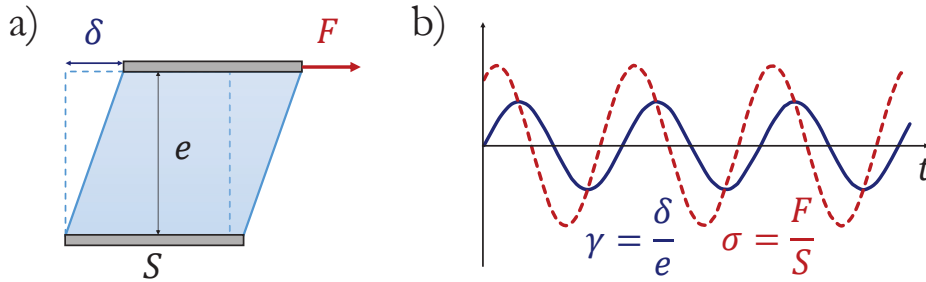


Figure 2.4: (a) Schematic view of shear rheology: the initial shape of the sample (dashed line) is a prism with base surface S and height e equal to the gap between the two confining surfaces (top and bottom plates). A sliding force F is applied to one of the two surfaces, while the other one is kept fixed. This corresponds to a shear couple $M = eF$, and a scalar shear stress $\sigma = F/S$ homogeneously distributed inside the sample volume. The scalar deformation $\gamma = \delta/e$ is also uniform, and corresponds to the relative displacement of the two surfaces δ normalized by the gap. (b) Representative experimental protocol for strain-controlled small amplitude oscillatory shear rheology: as described in text, a sinusoidal deformation $\gamma_\omega(t)$ (blue, solid line) is imposed, and the stress response $\sigma_\omega(t)$ (red, dashed line) is measured. The relative amplitude and phase of the two harmonic signals define the modulus and the phase of the complex modulus $G^*(\omega)$. The result would be the same in stress-controlled rheology, where $\sigma_\omega(t)$ is imposed and $\gamma_\omega(t)$ is measured.

Experimentally, it is possible to access both $\sigma(t)$ and $\gamma(t)$ using sophisticated instruments called rheometers, which can be controlled either in stress or strain. In both cases the geometry can be chosen according to the properties of the sample: liquid-like samples are typically tested in a Couette cell, where the sample fills the gap between two coaxial cylinders, one of which rotates with respect to the other. Solid-like samples, on the other hand, are generally confined between a flat, fixed surface and a cone that is rotated to apply a given deformation (cone-plate geometry). In both cases, strain-controlled

rheometers measure the torque needed to achieve a given rotation, and conversely stress-controlled rheometers apply a controlled torque and measure the rotation. The geometric parameters are then used to convert the torque into a shear stress and the rotation angle into a shear strain. Different shear geometries, like parallel sliding plates are also employed in custom-made shear cells, typically designed to meet special mechanical requirements (e.g. very small sample thickness or very high frequencies) or to be embedded into more complex experimental systems, like the one that will be presented in chapter 3.

When an external shear stress $\sigma(t)$ is applied to a sample, the sample reacts with a shear deformation $\gamma(t)$ following Newton's second law. If inertial effects can be ignored, as is often the case (cf. chapter 3), the internal stresses developed as a consequence of the shear deformation are such that the applied stress is exactly balanced, so that a measure of $\gamma(t)$ for a known stress history $\sigma(t)$ allows one to extract the constitutive equation. Conversely, a strain history $\gamma(t)$ can be imposed, and a measure of $\sigma(t)$ allows the same constitutive equation to be obtained.

As an example of a simple constitutive equation, Hooke's law describes the behavior of elastic solids, for which stress is always directly proportional to strain but independent on the shear rate $\dot{\gamma} = d\gamma/dt$. On the other hand, the classical theory of hydrodynamics deals with viscous liquids, for which stress is always directly proportional to the shear rate, but independent of the strain itself. Both categories are idealizations, and although many solids approach Hooke's law for small strains and many liquids approach Newton's law for small shear rates, under other conditions deviations from these simple, linear laws are observed. Moreover, even if the strain or the shear rate are infinitesimal, a system may exhibit behavior which combines liquid-like and solid-like characteristics: to describe such a *viscoelastic* system, a more general model must be introduced.

2.2.2 Linear viscoelasticity

2.2.2a Viscoelastic moduli

As a starting point for a theoretical description of linear viscoelasticity, a response function $G^*(\omega)$ (called complex modulus) can be defined, in the spirit of Sec. 2.1. In the small perturbation limit, the so-called linear regime, $G^*(\omega)$ is a well defined complex function of frequency: a harmonic strain perturbation $\gamma_\omega(t) = \gamma_0 e^{i\omega t}$ is associated to a stress $\sigma_\omega(t)$ oscillating at the same frequency ω , with amplitude and phase set by the complex modulus: $\sigma_\omega(t) = G^*(\omega)\gamma_\omega(t)$ (Fig. 2.4b) [Macosko 1994].

The ideal cases of purely elastic or viscous materials can be described in terms of real or imaginary complex moduli, respectively: $G^*(\omega) = G_0$ defines the elastic modulus in Hooke's law ($\sigma = G_0\gamma$), whereas $G^*(\omega) = i\omega\eta$ characterizes the viscosity of a Newtonian liquid ($\sigma = \eta\dot{\gamma}$). A complex modulus having both a real and an imaginary part describes a viscoelastic material, whose solid-like and liquid-like behaviors are ascribed to a storage modulus $G' = \text{Re}(G^*)$ and a loss modulus $G'' = \text{Im}(G^*)$, respectively. In practice,

oscillatory rheology consists in imposing a small amplitude harmonic perturbation (either in stress or in strain), and recording the amplitude and phase of the response, from which G' and G'' can be extracted for a given frequency: a complete spectrum of $G'(\omega)$ and $G''(\omega)$ provides a full description of the linear viscoelasticity of a material.

The form of the frequency dependence of the viscoelastic moduli G' and G'' can in general be reproduced by the behavior of a mechanical model with a sufficient number of elastic elements (springs) and viscous elements (dashpots imagined as pistons moving in oil). The force applied to the ends of this mechanical model is analogous to σ , and their relative displacement is analogous to γ . The simplest fully viscoelastic models contain one spring and one dashpot, connected either in series (Maxwell model) or in parallel (Kelvin-Voigt model) [Ferry 1980]. Their complex moduli can be calculated by assigning an elastic modulus G_0 to the spring and a viscosity η to the dashpot, and by developing the mechanical models, obtaining $G_{KV}^*(\omega) = G_0 + i\omega\eta$ for Kelvin-Voigt and $G_M^*(\omega) = G_0(s^2 + is)/(1 + s^2)$, with $s = \omega\eta/G_0$, for Maxwell. Both results are represented in Fig. 2.5a, from which a characteristic angular frequency $\bar{\omega} = G_0/\eta$ emerges as the point where G' and G'' cross each other: for $\omega > \bar{\omega}$ the Maxwell model will be predominantly elastic, with $G' > G''$, whereas for Kelvin-Voigt $G'' > G'$ indicates a rather liquid-like response. The opposite holds for $\omega < \bar{\omega}$.

The characteristic frequency $\bar{\omega}$ can also be read, in the time domain, as a characteristic time $\tau \sim \bar{\omega}^{-1}$ separating the elasticity-dominated from the viscosity-dominated regime, as can be clearly observed in transient experiments.

2.2.2b Transient experiments in the linear regime

Oscillatory shear is of widespread use, and is an extremely practical tool to characterize the linear viscoelasticity of a material, since it probes a stationary state, where the mechanical response of the system depends on frequency but not (or negligibly) on time. However, precious physical information is often contained as well in the time evolution of the system approaching the stationary state, specially when finite, "nonlinear" deformations are attained. To access this information, transient experiments, intrinsically time-resolved, can be performed. Creep, shear start-up and stress relaxation are the most common examples of transient rheological experiments.

The result of transient experiments in the linear regime can be rationalized in terms of two time-dependent quantities related to the viscoelastic moduli: the stress relaxation modulus $G(t)$ and the creep compliance $J(t)$, which are used to calculate the stress $\sigma(t)$ starting from a generic strain history $\gamma(t)$ or vice versa [Macosko 1994]. Their definition is based on Boltzmann's superposition principle, stating that in the linear regime the effects of sequential changes in strain (or stress) are additive:

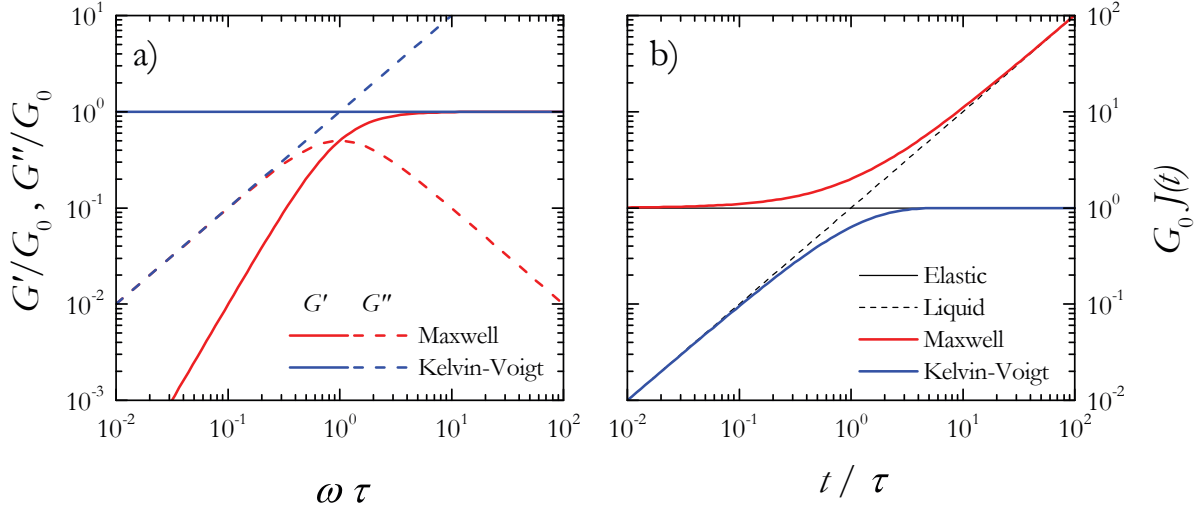


Figure 2.5: (a) Viscoelastic moduli G' (solid lines) and G'' (dashed lines) for Maxwell (red) and Kelvin-Voigt model (blue), normalized by the spring modulus G_0 and as a function of frequency normalized by the relaxation time $\tau = \eta/G_0$. A solid sample would have the same G' as the Kelvin-Voigt ($G' = G_0$), whereas a Newtonian fluid would have the same G'' as the Kelvin-Voigt ($G'' = \eta\omega$). (b) Normalized creep compliance $G_0J(t)$ as a function of normalized time t/τ for the two viscoelastic models. As a reference, the creep compliance of ideal elastic solids (black, solid line) and Newtonian liquids (dashed line) is also shown.

$$\sigma(t) = \int_{-\infty}^t G(t-t')\dot{\gamma}(t')dt' \quad (2.16)$$

$$\gamma(t) = \int_{-\infty}^t J(t-t')\dot{\sigma}(t')dt'$$

From the knowledge of either $G(t)$ or $J(t)$, the stress-strain relation for any kind of experiment with a prescribed time dependence of stress or strain can be predicted: for example, the particular choice of an oscillating strain allows one to identify the complex modulus $G^*(\omega)$ as the Fourier transform of $G(t)$. In practice, however, direct calculation of the Fourier transform is not possible, since any transient experiment accesses a limited window of timescales, ranging from a generally small enough t_{min} to a maximum time t_{max} limited by the duration of the experiment (typically a few days at most), and numerical methods are needed to convert linear transient data into viscoelastic moduli covering a frequency range from $\omega_{min} \sim t_{max}^{-1}$ to $\omega_{max} \sim t_{min}^{-1}$ [Evans 2009]. This reveals another side advantage of transient experiments, which can typically probe a much larger window of timescales, beyond the small frequency regime that can be typically be accessed in

oscillatory tests. For this reason, creep or stress relaxation experiments in the linear regime are sometimes used to extend the spectrum of viscoelastic moduli at the smallest frequencies [Bird 1987].

Among the typical transient experiments, this chapter discusses the case of creep, where a step stress $\sigma(t) = \sigma_0\theta(t)$ is imposed, $\theta(t)$ being the Heaviside's Theta function, and the strain $\gamma(t) = \sigma_0J(t)$ is measured as a function of time. Apart from inertial effects, discussed in detail in chapter 3, the deformation is constant ($\gamma(t) = \gamma_e = \sigma_0/G_0$) for an ideal elastic solid subject to Hooke's law, whereas it grows linearly in time for a viscous liquid ($\gamma(t) = \dot{\gamma}t$, where $\dot{\gamma} = \sigma_0/\eta$). The deformation of a Maxwell model is approximately constant over times shorter than the characteristic time τ , and starts growing at a constant rate for longer times: $\gamma_M(t) = \gamma_e(1 + t/\tau)$. On the other hand, a Kelvin-Voigt model flows at short times and reaches a constant deformation for $t \gg \tau$: $\gamma_{KV}(t) = \gamma_e[1 - \exp(-t/\tau)]$. Both creep curves are represented in Fig. 2.5b.

The reversibility of creep deformation can be directly addressed by creep recovery, i.e. by releasing the external stress after an arbitrary creep time T : for $t > T$ the deformation $\gamma(t)$ decreases again, reaching a plateau value γ_∞ in the long time limit. $\gamma_\infty = 0$ would then imply that the deformation obtained during creep is completely reversible: this is the case of Kelvin-Voigt model. On the other hand, a partially irreversible deformation would reflect into a strictly positive γ_∞ (for example, $\gamma_\infty = \gamma_e T/\tau$ for a Maxwell model).

The two fully viscoelastic models (Maxwell and Kelvin-Voigt) introduced so far are described by a single characteristic time τ , corresponding to the clear transition between solid-like and liquid-like behavior, which one can observe in Fig. 2.5b. However, as the term "creep" itself suggests, the deformations observed in creep experiments are often characterized by a sublinear growth of $\gamma(t)$ spanning several decades in time. This is for example the case of Rouse motion in polymeric materials, where $\gamma(t)$ increases as a power law with an exponent $\alpha = 0.5$ [Schiessel 2000]. To mimic this behavior more complex mechanical models are required, generally displaying a distribution of relaxation times. For example, a generalized Maxwell (or Kelvin-Voigt) model is composed of N elementary modes, each one with its characteristic time, connected in series (or in parallel). Other models can be imagined as well, like for example branched or nested structures, particularly suited to describe self-similar dynamics. More recently, the concept of fractional element (also called a springpot) has also been introduced [Blair 1947], to provide a compact mathematical description of power law distributions of relaxation times [Bagley 1983, Bagley 1989, Jaishankar 2013]. A fractional element is defined by two parameters: a so-called *quasi-property* \mathbb{V} and a fractional exponent α , and it bridges the mechanical behavior of a spring and a dashpot, where (\mathbb{V}, α) reduces to $(G_0, 0)$ and $(\eta, 1)$ respectively. Its constitutive equation involves the concept of a fractional derivative of order α :

$$\sigma(t) = \mathbb{V} \frac{d^\alpha \gamma}{dt^\alpha} = \mathbb{V} \int_{-\infty}^t (t-t')^{-\alpha} \dot{\gamma}(t') dt' \quad (2.17)$$

This definition of fractional derivative compared with Eq. 2.16 allows to identify the relaxation modulus $G(t) \propto t^{-\alpha}$, which emphasizes the interpretation of a springpot in terms of a power law distribution of relaxation times. A physical example of such a fractional element is represented by the so-called fractional Maxwell model, which will be introduced in chapter 5.

2.2.3 Nonlinear viscoelasticity

All the results obtained so far are bound to the underlying assumption that the deformations are infinitesimal. This assumption characterizes the so-called linear viscoelastic regime, where stress and strain should be regarded as a probing field: since the (linear) response functions do not depend on the magnitude of the probing field, linear rheology teaches us about the mechanical properties of the *unperturbed* sample. However, from a practical point of view, it may remain unclear how to identify the range of deformations where this assumption holds. Moreover, mechanical stimuli beyond the linear regime can be used on purpose to change the sample structure, and the mechanical properties of the modified structure can be probed by nonlinear rheology, which can provide valuable information both from a fundamental point of view and for applications. For this reason, in this section a few relevant aspects of nonlinear viscoelasticity will be briefly discussed.

Nonlinear rheology represents an appealing technique thanks to its straightforward implementation in modern rheometers. However, from a theoretical point of view it is extremely delicate, for several reasons. First of all, when strains are not infinitesimal, the strain tensor itself has to be handled with care, since various alternative ways of defining finite strains are possible [Macosko 1994]. Moreover, the deformation measured macroscopically may deviate significantly from the local deformation actually experienced by the sample, which may become unstable and heterogeneous in a way that may exhibit a delicate dependence on the experimental geometry and boundary conditions. Finally, as a consequence of a nontrivial coupling between spatial dimensions, nonlinear deformations along one direction may produce measurable stresses along orthogonal directions, as is the case for normal stresses in shear rheology, for example. A thorough discussion of those aspects would go far beyond the purpose of this chapter: in the following we will take a phenomenological approach, assuming that a macroscopic shear strain γ is imposed and a macroscopic shear stress σ is measured under specific experimental conditions. Under the working hypothesis (to be verified experimentally) that γ and σ are still representative of the local mechanical perturbation and response of the sample, this section will discuss how the stress-strain relation changes as the strain is increased beyond the linear regime.

2.2.3a Large Amplitude Oscillatory Shear

We start considering the nonlinear transition as it is observed in oscillatory shear at one fixed frequency ω as the strain amplitude γ_0 is increased. For one given γ_0 , a convenient way of showing the stress-strain relation is to plot the two variables against